Arsenic in hydrothermal apatite: oxidation state, mechanism of uptake, and comparison between experiments and nature

Weihua Liu[1*], Yuan Mei[1,2], Barbara Etschmann[2], Joël Brugger[2], Mark Pearce[1], Chris G. Ryan[1], Stacey Borg[1], Jeremey Wykes[3], Peter Kappen[3], David Paterson[3], Ulrike Boesenberg[4], Jan Garrevoet[4], Gareth Moorhead[1], and Gerald Falkenberg[4]

[1]CSIRO Mineral Resources, Clayton, Vic 3168, Australia

[2]School of Earth, Atmosphere and the Environment, Monash University, Clayton, Vic 3168, Australia

[3]Australian Synchrotron, Clayton, Vic 3168, Australia

[4] Deutsches Elektronen Synchrotron, DESY, Notkestr. 85, D-22607 Hamburg, Germany

Corresponding author: weihua.liu@csiro.au

Abstract

Element substitution that occurs during fluid-rock interaction permits assessment of fluid composition and interaction conditions in ancient geological systems, and provides a way to fix contaminants from aqueous solutions. We conducted a series of hydrothermal mineral replacement experiments to determine whether a relationship can be established between arsenic (As) distribution in apatite and fluid chemistry. Calcite crystals were reacted with phosphate solutions spiked with As(V), As(III), and mixed As(III)/As(V) species at 250 ˚C and water-saturated pressure. Arsenic-bearing apatite rims formed in several hours, and within 48 hours the calcite grains were fully replaced. X-ray Absorption Near-edge Spectroscopy (XANES) data show that As retained the trivalent oxidation state in the fully-reacted apatite grown from solutions containing only As(III). Extended X-ray Fine Spectroscopy (EXAFS) data reveal that these As(III) ions are surrounded by about three oxygen atoms at an As-O bond length close to that of an arsenate group (AsO_4^{3-}), indicating that they occupy tetrahedral phosphate sites. The three-coordinated As(III)-O_3 structure, with three oxygen atoms and one lone electron pair around As(III), was confirmed by geometry optimization using *ab initio* molecular simulations.

The micro-XANES imaging data show that apatite formed from solutions spiked with mixed As(III) and As(V) retained only As(V) after completion of the replacement reaction; in contrast, partially reacted samples revealed a complex distribution of As(V)/As(III) ratios, with As(V) concentrated in the center of the grain and As(III) towards the rim. Most natural apatites from the Ernest Henry Iron Oxide Copper Gold deposit, Australia, show predominantly As(V), but two grains retained some As(III) in their core. The As-anomalous amphibolite-facies gneiss from Binntal, Switzerland, only revealed As(V), despite the fact that these apatites in both cases formed under conditions where As(III) is expected to be the dominant As form in hydrothermal fluids.

These results show that incorporation of As in apatite is a complicated process, and sensitive to the local fluid composition during crystallization, and that some of the complexity in As zoning in partially reacted apatite may be due to local fluctuations of As(V)/As(III) ratios in the fluid and to kinetic effects during the mineral replacement reaction. Our study shows for the first time that As(III) can be incorporated into the apatite structure, although not as efficiently as As(V). Uptake of As(III) is probably highly dependent on the reaction mechanism. As(III)O_3^{3-} moieties replace phosphate groups, but cause a high strain on the lattice; as a result, As(III) is easily exchanged (or oxidized) for As(V) during hydrothermal recrystallization, and the fully

reacted grains only record the preferred oxidation state (i.e., As(V)) from mixed-oxidation state solutions. Overall this study shows that the observed oxidation state of As in apatite may not reflect the original As(III)/As(V) ratio of the parent fluid, due to the complex nature of As(III) uptake and possible *in-situ* oxidation during recrystallization.

Keywords: apatite, arsenic, oxidation state, mineral replacement reaction, XANES spectroscopy, molecular simulations, trace element partitioning.

Highlights

- As(III) and As(V) both can be incorporated in hydroxylapatite during dynamic coupled dissolution/reprecipitation reactions.
- As(III) moieties replace phosphate groups with a high local strain compared to As(V).
- Upon recrystallization, As(V) replaces the As(III) in the hydroxylapatite structure.
- Most studied natural apatites retain mainly As(V), even though they formed from solutions that mainly contained As(III).
- Reaction pathway and kinetics exert a major controls on As(III) uptake in apatite.

1. Introduction

The apatite group, with its general formula of $A_{10}(XO_4)_6(F, OH, Cl)_2$; A = Ca, Sr, Ba, Pb, ± Na, REE on two different crystallographic sites; X = P^{5+}, As^{5+}, V^{5+}, Si^{4+} on a rigid tetrahedral site; and F, Cl, OH^- (so-called 'column anions') located within channels down the *c*-axis; plays an important role in various geological, industrial, and biological processes (e.g. Pan and Fleet, 2002;

Pasero et al. 2010; Hughes and Rakovan, 2015). Apatite-group minerals are widespread accessory minerals in many rock types, accounting for a large part of P mass balance, but also hosting significant amounts of other key petrologically and environmentally significant elements such as F, Sr, As, U, or REE. The ability of apatite to scavenge toxic metals such as As or U forms the basis of its use in environmental remediation and waste disposal, and apatite is probably the most important biomineral of relevance for human health.

Trace element substitutions in apatite can be used to investigate the nature of geological fluids from which the apatite precipitates or by which the apatite has been altered (e.g., Harlov 2015). Tracing the origin of the observed zonation and interpreting it in terms of fluid-rock interaction is fundamental to understanding how metals are transported and deposited. In particular, the trace element zonation observed in hydrothermal apatite may be used to track fluid chemistry (Bath et al. 2013), and help mineral exploration (Mao et al., 2016).

Studies of As incorporation in apatite also have applications for As mobility and treatment in environmental and industrial systems. Arsenic can be released into an aqueous phase from As-bearing minerals during various processes such as weathering and mining (Alam et al. 2014; Jamieson et al. 2011). Many approaches have been developed to remove As from water, including chemical reactions to form As-bearing minerals, adsorption of As onto mineral surfaces, and co-precipitation of As into mineral structures (Choong et al., 2007, Renard et al., 2015). For example, lime has been used to immobilize As in wastewater due to the formation of arsenate apatite instead of calcium arsenate (Bothe and Brown, 1999).

Arsenic has eight oxidation states from -3 to +5, and As(III) and As(V) are the main species in aqueous solutions depending on oxygen fugacity, pH and temperature (Testemale et al., 2004; James-Smith et al., 2010; Qian et al. 2013; Renard et al., 2015). Arsenic(V) exists mainly as charged tetrahedral arsenate complexes (e.g., $H_2AsO_4^-$ and $HAsO_4^{2-}$) in natural waters, whereas due to a stereochemically active lone electron pair, As(III) exists mainly as a neutral trigonal pyramidal $As(OH)_3(aq)$ complex, with three oxygen on the basal plane and As on the apex (Testemale et al., 2004). As the arsenate (AsO_4^{3-}, As-O distance ~1.69 Å) and phosphate (PO_4^{3-}; P-O distance ~1.53 Å) moieties share a similar tetrahedral geometry, phosphate groups in solids can be substituted by arsenate groups, despite large differences in ionic radii of the P^{5+} (0.17 Å) and As^{5+} (0.34 Å) cations.

Several studies have investigated As(V) incorporation in apatite; most are characterization of As-bearing apatite synthesized from stoichiometric reactions of chemical compounds (e.g., Lee

et al., 2009; Zhu et al. , 2009; Zhang et al., 2011). They found that a complete solid solution series can be formed between hydroxylapatite ($Ca_5(PO_4)_3OH$) and johnbaumite ($Ca_5(AsO_4)_3OH$). A recent study investigated the process of As substitution during the calcite – apatite replacement reaction under hydrothermal conditions (Borg et al., 2014). This study showed that arsenate (AsO_4^{3-}) moieties from the solution are rapidly (within an hour) taken up by apatite, initially resulting in a complex zoning pattern of As within the apatite structure. Within two days the zoning disappears and a homogeneous As-bearing hydroxylapatite forms as the final product. Borg et al. (2014) show that the uptake of As and the chemical zoning in apatite formed via calcite replacement are controlled by the local fluid-mineral equilibrium (see Putnis, 2009; Altree-Williams et al. 2015). So far to the authors' knowledge there is no report on As(III) substitution in apatite-group minerals.

The aim of this paper is to investigate the uptake of As in hydroxylapatite from solutions containing both As(III) and As(V), and the effects of the different As oxidation states in solution on the zoning and composition of the resulting hydroxylapatite (we will use 'apatite' for the 'hydroxylapatite' for the rest of the paper). Both As(III) and As(V) were incorporated in apatite formed via hydrothermal replacement of calcite at 250 ºC. We used synchrotron micro-XANES, bulk XAS and SEM techniques to determine and map element distribution and the oxidation state of As in the hydrothermally synthesized As-bearing apatite, as well as in natural hydrothermal apatite from the Ernest Henry iron oxide copper gold deposit, Queensland, Australia, and from an As-anomalous amphibolite-facies gneiss from Binntal, Switzerland. *Ab initio* molecular simulations were used to help constrain the coordination structure of As(III) and As(V) in apatite, and the substitution mechanism of different oxidation states of As in apatite.

2. Material and methods

2.1. Hydrothermal synthesis of As-bearing apatite

Arsenic-bearing apatite grains were synthesized by reacting calcite crystals with As(III)- and As(V)-bearing phosphate solutions at 250 ºC in a titanium cell that had been preheated to 380 ºC to form a thin inert TiO_2 layer on the surface. Three series of experiments were conducted aiming to incorporate As(V), As(III) and mixture of As(V) and As(III) into apatite (Table 1): in Series V the starting solutions are a mixture of sodium arsenate and phosphate solutions with 0.12 m As(V) concentration (Borg et al., 2014); in Series III the starting solutions are phosphate

143 solutions spiked with 0.03-0.14 m As_2O_3; and in Series M the starting solutions contain mixtures
144 of different concentrations of As_2O_3 and sodium arsenate to get variable As(III)/As(V) ratios. The
145 solution $pH_{250°C}$ ~5.6, calculated based on geochemical modelling package HCh and default
146 thermodynamic database (Shvarov, 2008).

147 For each experiment, the solutions were purged with N_2 gas before sealing the Ti cell to
148 remove the air; during the experiments the solution was only in contact with the inner wall of the
149 Ti cell. For each series, a few short runs of 3-5 hours were conducted to achieve partial replacement
150 of calcite by apatite, and longer runs of 48 hours to obtain complete replacement, as indicated in
151 Borg et al. (2014).

152 **2.2. Natural hydrothermal apatite from Ernest Henry IOCG deposits, NT, Australia**

153 The Ernest Henry Fe-oxide-Cu-Au (IOCG) deposit is located in the Eastern Succession of
154 the Mount Isa Inlier, Queensland, Australia. The deposit is a mineralised breccia hosted in
155 volcanics within the Mary Kathleen Group. The mineralisation comprises chalcopyrite, pyrite,
156 electrum and magnetite associated with calcite and apatite and the ore-zone is surrounded by a
157 100 m-scale zone of K-metasomatism that overprints earlier regional Na-Ca alteration. Ore-
158 minerals are located between clasts of K-feldspar-altered volcanics. Fluid inclusion studies
159 indicate the presence of hyper-saline brines with a distinct magmatic component (Mark et al. 2005)
160 that provide an effective transport medium for large amounts of K and metals. Reactive transport
161 modelling indicates that whilst many of the alteration assemblages observed at Ernest Henry can
162 be produced by fluid-rock reaction with a hypersaline brine, mixing of a second fluid is required
163 to reproduce the voluminous calcite-bearing assemblages (Cleverley and Oliver 2005).

164 Apatite from Ernest Henry is enriched in fluorine and As (Rusk et al. 2010) compared to
165 other IOCG deposits. Individual grains are zoned with respect to As and S and contain up to 5 and
166 0.5 wt% respectively (Cleverley 2006). The sample analysed in this study comes from the upper
167 ore zone of the Ernest Henry mine. It contains pyrite, apatite, hematite, and quartz with minor
168 magnetite and calcite. The apatite is irregularly zoned in As, with As-poor cores and a series of
169 variably well-developed As-bearing rims with up to several percent of As concentrations.

170 **2.3. Apatite from As-anomalous amphibolite-facies gneiss from Binntal, Switzerland**

171 The Binntal Valley (Central Alps, Switzerland) is a hot spot of mineral diversity, being the
172 type locality for forty-three new mineral species, many of which contain As. Gneisses (including

meta-rhyolites) from the Monte Leone Nappe (Brianconnais Domain) are a likely As source for the numerous small-scale hydrothermal and metamorphic-hydrothermal As-bearing mineralization occurrences in the Valley (e.g., Lengenbach metamorphosed sedimentary exhalative deposit, and the As-REE-Ti-rich minerals in the alpine vugs of Monte Cervandone; Knill, 1996). The studied sample is a quartz-K-feldspar-muscovite±biotite gneiss from Ritterpass (Cuchet et al. 2014). The Monte Leone Nappe has experienced Barrovian style, medium temperature and pressure amphibolite facies metamorphism during the Neoalpine period (≤ 30 Ma). Apatite in this sample occurs within the main schistosity, which formed at peak temperatures 450-580˚C (Carrupt, 2003; Gregory, 2012). The sample also contains a folded quartz-K-feldspar vein with a cm-sized As-Nb-REE-bearing titanite (Cuchet et al. 2014).

2.4. Synchrotron bulk XAS measurement

Arsenic K-edge X-ray absorption spectroscopic (XAS) measurements of bulk samples were conducted at the XAS beamline of the Australian Synchrotron (AS). The AS storage ring operated in top-up mode with beam current of 200 mA. The XAS beamline has a 1.9 T wiggler source, and a Si(111) monochromator was used for As K-edge measurement with an energy resolution of 1.5 $x10^{-4}$ at 10 keV. The size of the X-ray beam on the sample was 0.5 mm (V) x 1 mm (H). The samples were ground to powder and sealed with Kapton tape, and XANES and EXAFS data were collected under ambient conditions in fluorescence mode with a Canberra 100-element Ge detector.

2.5. Synchrotron µ-XRF and µ-XANES imaging

Elemental mapping and As K-edge XANES imaging (Etschmann et al. 2010; 2014) was performed for the partially reacted apatite samples and natural apatite from Ernest Henry and Binntal. The synthesized apatite grains (0.5- 3 mm diameter) were mounted on a quartz slide and polished to ~30 µm thickness for optimal Synchrotron µ-XRF measurement. The ore samples from Ernest Henry and Binntal were also prepared into 30 µm thin sections on quartz slides.

Elemental maps and XANES stacks were measured at the X-ray fluorescence microscopy (XFM) beamline (Paterson et al., 2011) at Australia Synchrotron. Details of the measurement procedure and data reduction are found in Li et al. (2016) and Etschmann et al. (2014). The Si(111) monochromator delivers an energy resolution ΔE/E of ~2.8 x 10^{-4}, and the beam was focused to a ~2 µm spot size using Kirkpatrick-Baez mirrors. Fluorescence data were collected using the Maia

model C 384 detector array, which has an energy resolution of 240 eV and can detect elements down to atomic number 15 (phosphorous) (Ryan et al. 2014; Kirkham et al., 2010). Samples were mapped using different scanning speeds (1.024 to 2.048 mm/s), corresponding to dwell times of 2 to 12 ms/pixel. The MSXRF data were analyzed with the GeoPIXE software package (Ryan et al., 1990, 2010b), using standard foils (Pt, Mn, Fe) as external standards as well as Ca as an internal standard (from calcite starting material) to constrain the quantification parameters (detector geometry and efficiency; calibration of ion chamber to measure photon flux). The method uses the Dynamic Analysis (DA) method (Ryan et al., 1993, 2000, 2010a) to deconvolute the spectral components due to As and other elements from elastic and inelastic scattering. A separate DA matrix is used for each beam energy stack to track the changing energy of the scatter peaks. The result is a 3D data cube providing As XANES spectrum at each pixel position.

SXRF maps were collected at eighty-seven irregularly spaced monochromator energies that spanned the As-K edge, averaging 1 eV per step, with 0.5 eV steps across the edge. The As concentrations at each pixel in the SXRF map, at each monochromator energy, were extracted and used to construct XANES spectra at each pixel. These XANES spectra were normalized and smoothed using box-car smoothing over 2x2 pixels and then the resulting XANES spectra were fitted using a linear combination of As_2O_3 and $Na_2HAsO_4{\bullet}7H_2O$. The resulting linear fitting components were normalized to one and As(III)/As maps were generated (Etschmann et al. 2010; 2014). An overview map of each sample was performed covering areas of about 130 mm2 at 4 µm pixel pitch (typically 4500 x 1700 pixels) with a transit time of 1 ms per pixel. Regions of interest were selected from these overviews for detailed XANES mapping. These XANES stacks comprised image frames (typically 250 x 150 pixels) at 10 µm pitch and 4.9 ms transit per pixel, repeated over a sequence of 181 energies spanning the K absorption edge of As. The data was analyzed as described above.

A detailed XANES data cube on one sample was also acquired at the P06 beamline at the PETRA III synchrotron at DESY (Schroer et al., 2010). This experiment also used a Maia model C detector, but benefitted from a finer beam resolution (~0.4 µm), a monochromator energy resolution $\Delta E/E$ of ~1.4×10^{-4} and scanning of the energy axis as the fast axis to provide uniformly fine energy steps (0.5 eV at 1 ms/step).

2.6. Assessment of beam damage and As oxidation due to sample preparation

Arsenic is known to be susceptible to synchrotron X-ray beam damage, depending on sample type, concentration, type of the X-ray source, and photon flux density (Smith et al., 2005). For example, As(III) in solution may be oxidized to As(V) due to beam damage (e.g., James-Smith et al., 2010). Time-dependent measurements show that for bulk XAS analyses conducted at room temperature, no beam damage is observed for the arsenolite (As_2O_3) standard and all As(V) samples. For the As(III) apatite samples, there is slight beam damage (1.1% oxidized to As(V) based on linear combination fit) among repeated scans lasting 35 minutes. For the micro-XANES measurement, it is more difficult to assess the extent of the beam damage and oxidation of As during the preparation of thin sections; however it is suggested that this is not a significant issue, as pure As(III) and mixed As(III)/As(V) spectra were retrieved from the XANES maps for mixed As(III)/As(V) samples, and only qualitative interpretations are made from the measured spectra. Significant beam damage is unlikely for micro-XANES measurement, because the dwell time is very low (12 ms).

2.7. *Ab initio* molecular simulations

Structure optimizations of arsenolite, hydroxylapatite and hydroxylapatite substituted with As(V) and As(III) were carried out using density functional theory (DFT) within the CPMD code (version 3.17.1, Car and Parrinello, 1985). The DFT-based *ab initio* simulations have been successfully used to simulate the structure of hydroxylapatite (Slepko and Demkov, 2011), and cations substitution in hydroxylapatite (e.g., Terra et al., 2009; Zeglinski et al., 2012).

The CPMD method implements DFT using plane-wave basis sets and pseudopotentials to simulate the presence of the core electrons and the nucleus. In this study, the BLYP (Becke, Lee, Yang and Parr) exchange correlation-functional was employed (Lee et al., 1988; Becke, 1988) together with Martins–Troullier pseudo-potentials (plane-wave cutoffs of 80 Ry) from the CPMD package (Troullier and Martins, 1991). In each calculation, wavefunction optimization was conducted initially and then followed by geometry optimization. Convergence criteria of 10^{-5} and 10^{-3} were applied for wavefunction and geometry optimization, respectively. All calculations were conducted using periodic boundary conditions.

Geometry optimization of arsenolite (As_2O_3) was performed with a single unit cell containing 80 atoms (crystal structure refinement of Ballirano and Maras, 2002). Calculations with up to 12 super-cells of hydroxylapatite (crystal data from Wilson 1999; 44 atoms per unit cell;

263 [$Ca_5(PO_4)_3OH$], Z = 2) were conducted to test the effect of super-cell size. The cells were aligned
264 in the order of 1-1-1, 1-1-2, 1-1-3, 2-2-2 and 2-2-3 along a-b-c dimension; where 1-1-1 is defined
265 to be the unit cell, 1-1-2 is defined to consist of the unit cell plus a second unit cell along the c
266 axis, 2-2-3 consists of 2 unit cells along a, 2 unit cells along b and 3 unit cells along c, etc. The
267 unit cell size was kept constant for all calculations, which is consistent with the low concentration
268 of As substituted into the apatite (≤2.5 wt% As). As the geometrical properties of the 1-1-3 super-
269 cell (132 atoms) and 2-2-3 (528 atoms) gave a similar agreement between the optimized bond
270 distances and the measured values of Wilson (1999), the super-cell 1-1-3 was chosen for geometry
271 optimization of As-substituted hydroxylapatite. Series of calculations were performed with As
272 substitution in different oxidation states: i) As(V)-substituted hydroxylapatite (132 atoms in a 1-
273 1-3 super-cell with one AsO_4^{3-} replacing one PO_4^{3-}, corresponding to 2.45 wt% As; and ii) As(III)-
274 substituted hydroxylapatite (131 atoms in a 1-1-3 super-cell with one AsO_3^{3-} moiety replacing one
275 PO_4^{3-} group). Four different possibilities of replacing PO_4^{3-} by AsO_3^{3-} were calculated by removing
276 each of the four oxygen atoms in the PO_4^{3-} site.

277 # 3. Results

278 ## 3.1. Arsenic oxidation state in apatite as a function of reaction progress and As(III)/As(V)
279 ratio in the mother solution

280 All the short (3-5 hour) experimental runs resulted in calcite grains with an As-bearing
281 apatite rim, and the 48 hour runs ended up with complete replacement of calcite by As-bearing
282 apatite. Micro-XANES maps were measured for the partially reacted samples from the mixed
283 As(III)/As(V) solutions, and bulk XANES and EXAFS data were collected for the fully reacted
284 (no calcite left) samples (Table 1).

285 As(V)-only experiment. Calcite crystals were reacted in the presence of solutions that
286 contained only As(V) (Sample V-2-8). The XANES spectrum (Fig. 1) shows only the spectral
287 features characteristic of As(V), consistent with substitution of As(V) for P(V) in the tetrahedral
288 PO_4^{3-} sites.

289 As(III)-only experiments. The bulk XANES spectra for the fully replaced samples from
290 solutions that contained only As(III) (1.3 m $(NH_4)_2HPO_4$ and variable amounts of dissolved
291 As_2O_3) show only the As(III) features (samples III-13-5 and III-13-6, Fig. 1), suggesting
292 substitution of As(III) in the apatite structure. There is a linear trend between the As concentrations

in the solid and the initial As concentrations in the fluid (Fig. 2) for both As(V) and As(III) experiments, with the $As_{solid}/As_{solution}$ ratio lower in the case of the As(III) solutions (ratio around 0.1) than in the case of As(V) (~0.2; Borg et al., 2014), indicating that As(III) incorporation in apatite is less effective than As(V) incorporation.

Mixed As(III)/As_S(V) experiments. For the *fully reacted samples* made from solutions that contained both As(III) and As(V) (samples M-5 – M-8, Table 1), the bulk XANES spectra show only the presence of As(V) in all three samples (Fig. 1), despite the fact that these samples have different As(III)/As(V) ratios in the initial solutions (M-5, M-6 and M-8, Table 1). Micro-XANES spectra for one of these samples (M-6, solution As(III)/As(V) ratio = 1) also shows predominantly As(V) (Fig. 3).

In contrast, the micro-XANES maps show heterogeneous distribution of As(III) and As(V) for *partially reacted* samples formed under the same conditions from solutions containing both As(III) and As(V) (samples M-7 and M-9; Table 1; Fig. 4-5). For example, As(V) is concentrated in the inner part, and As(III) is more abundant on the outer part of the reaction rim of sample M-7 (solution As(III)/As(V) ratio = 1, Fig. 4). The M-9 sample, which has the highest ratio of As(III) among the mixed oxidation state solutions (As(III)/As(V) = 10.5), also has the highest level of As(III) (Fig. 5). Similar to M-7, As(III) in M-9 is enriched preferentially around the edge, and As(V) is concentrated towards the center of grain (Fig. 5b, c). The micro-XANES imaging on the smaller area in the M-9 sample, performed at PETRA beamline P06, is consistent with the results collected at the Australian Synchrotron, although the As(III) and As(V) peaks are better resolved as a result of the finer energy resolution of the beamline (Fig. 5e, f).

3.2. Nature of arsenic in apatite formed via calcite replacement

Bulk EXAFS were recorded for the fully reacted samples, as well as the As(III) and As(V) compounds that were used in the preparation of the solutions (hydrated sodium arsenate $Na_2HAsO_4(H_2O)_7$ and arsenolite As_2O_3). The EXAFS fitting results conducted in both R and K space are similar within the quoted errors, and fit parameters from R space fitting are compiled in Table 2, and the fitted EXAFS spectra and their Fourier Transform are plotted in Fig. 6a-b. Fitting the EXAFS spectrum of the sodium arsenate with 4 oxygens yields an As-O bond length of 1.697(7) Å, similar to previously reported crystallographic values (average 1.688(4) Å, Ferraris and Chiari 1970). The fitted As-O distance for arsenolite (As_2O_3) is much longer at 1.805(4) Å than in the arsenate (Table 3); this value is similar to the literature values of 1.786(2) Å from the

single crystal X-ray crystal structure refinement (Ballirano and Maras 2002). Both fits gave a similar value of 0.88 for the scale factor S_o^2, which is used in the subsequent refinement of the samples described below.

Results of fitting the Fourier transform of the EXAFS data are given in Table 2. There are a number of interesting points to note. The As(III)-bearing samples (R13-5 and R9-6) can be fitted with approximately three oxygen atoms at a bond length of 1.69(1) (R13-5) and 1.70(1) (R9-6) Å. Calcium can be fitted at 3.19(4) and 3.21(3) Å; Attempts to fit As-O multiple scatterings did not improve the fit, as there are some multiple scattering interactions but they do not contribute enough intensity.

These distances are similar to the published As(V)-O bond length values of 1.68(1) Å for As(V) solid solutions in apatite (Lee et al., 2009), and to the As-O distances (average 1.685 Å) in the calcium arsenates measured by Catti and Ivaldi (1983). The XANES spectra clearly show that the predominant oxidation state of this sample is As(III); however the fitted bond length is much shorter than the measured As(III)-O bond distance of 1.805(4) Å in arsenolite (Table 2), and 1.786(2) Å from the single crystal X-ray crystal structure refinement (Ballirano and Maras 2002). These differences, combined with the fact that an As-Ca bond length can be fitted, clearly indicate that the As(III) observed in these samples is not hosted in arsenolite inclusions (arsenolite was used to prepare the starting solutions).

For the fully reacted samples from the mixed As(III)/As(V) solutions, for which the XANES spectra show only As(V) feature (Fig. 1), the EXAFS fits for both end-member samples (M-5 and M-8, Table 1) result in ~4 oxygens at an As-O distance of 1.68(1) Å, as expected for As-O bonds in As(V)-bearing apatite (1.68(1) Å, Lee et al., 2009). As-Ca distances could be refined at 3.27(2) and 3.67(5) Å. The As(V)-Ca distance is longer than the As(III)-Ca, 3.27 vs 3.20 Å.

3.3. *Ab initio* molecular simulations of As(III/V) in the apatite structure

We performed DFT geometry optimization on arsenolite and hydroxylapatite (model benchmarking) and hydroxylapatite substituted by both As(V) and As(III). The optimized structures are shown in Fig. 7-9 and bond distances are listed in Table 3.

The optimized geometry of arsenolite gives an average As(III)-O distance of 1.815 Å, longer than the distance of 1.786(2) Å from x-ray crystallography (Ballirano and Maras, 2002), and our EXAFS measurement 0f 1.805(4) Å (Table 2). Geometry optimization of hydroxylapatite

predicted a P(V)-O distances of 1.55-1.56 Å, slightly longer than the crystallographic distance of 1.542 Å (Wilson et al., 1999). In arsenolite there are three coordinated O around As(III), resulting in a pyramidal structure with lone electron pair on top of As(III) (opposite the O3 position; Fig. 7a). In contrast, the fourfold PO_4^{3-} structure in hydroxylapatite gives evenly distributed electrons in a tetrahedral arrangement. In As-substituted hydroxylapatite crystals, the As-O bond distances are longer that the P-O distances for both As(III) and As(V) (Table 3). The P-O distances are 1.55-1.56 Å in all the hydroxylapatite structures calculated in this study (Fig. 8b). In the As(V)-substituted hydroxylapatite, the calculation gave As(V)-O distances of 1.68-1.69 Å (Fig. 8b), which are consistent with the value of 1.68(1) Å obtained from the EXAFS data fitting. In the structure where one out of every 18 P(V) atoms was replaced by an As(V) ion, the topology and electron distribution are similar to hydroxylapatite, despite the longer As(V)-O distance (Figs. 8a,b), and also very similar to the configuration found in johnbaumite (Fig. 8c).

Arsenic(III)-substituted hydroxylapatite shows slightly longer As-O distances (1.74-1.76 Å) than As(V)-substituted hydroxylapatite (Fig. 9). Similar to the case for arsenolite, this distance is longer than the distance retrieved from EXAFS fitting (1.69-1.70 Å, Table 2), and As(III) forms pseudo-tetrahedral AsO_3^{3-} moieties, where the missing fourth oxygen is occupied by the lone electron pair (Fig. 7a,b). When replacing one tetrahedral PO_4^{3-} by one AsO_3^{3-} moiety, the lone pair can replace one of four different oxygen atoms, and therefore we calculated four different configurations for the substitution of AsO_3^{3-} in hydroxylapatite. These four configurations are shown in Figure 9, illustrating the different types of distortion imposed on the rings surrounding the columnar anion channels using the preferred topological representation of White and Dong (2003). Configurations (b-d) are topologically similar to apatite, but the coordination of one of the neighboring Ca1 ions is reduced from 6 to 5 due to the oxygen vacancy. Configuration (a) shows the largest distortion of the ring.

3.4. Arsenic speciation in natural apatite

The natural apatites investigated in this study both show zoning with respect to As, in general displaying a relatively As-poor core and a relatively As-rich rim (Figs. 10-13). This zoning is visible in backscattered electron images for the Ernst Henry samples (As concentration ranges from 0.2 to 3.5 %), but only on the µ-XRF maps for the Binntal sample, where the highest As concentrations are ~0.23%.

The μ-XANES measurements for the Binntal sample and most of the grains (20 of 22 grains measured) in EH-4 and EH545 from Ernest Henry show only As(V) (e.g., Fig. 10-11), but two grains in the EH-545 sample from Ernest Henry show an As(III) component (Fig. 12-13). In particular, one grain shows clear zonation of As(III) and As(V), with an As(III)-rich core and an As(V)-rich rim (Fig. 13).

4. Discussion

4.1. As(V) incorporation by apatite

Incorporation of As(V) in natural apatite is well established (e.g., Brugger and Gieré, 1999; Bath et al. 2013), with the tetrahedral AsO_4^{3+} arsenate group substituting for the tetrahedral PO_4^{3-} phosphate group (Pan and Fleet, 2002; Lee et al., 2009, Zhu et al. 2009) as a result of similar tetrahedral moiety and charge, in spite of its larger size: the ionic radius of As^{5+} is twice as large as that of P^{5+} (0.34 vs 0.17 Å; Shannon, 1976). Lee et al. (2009) showed that the structure of apatite can accommodate the large size of the tetrahedral site simply with an increase in unit cell volume, with little affect on the sizes of Ca polyhedral, resulting in a complete solid solution with johnbaumite. The incorporation of minor amounts of As changes the physical properties of apatite; for example the solubility of As(V)-bearing apatite is higher than that of As-free apatite (Zhang et al., 2011). In our earlier study (Borg et al., 2014), we reacted calcite crystals with As(V)-bearing phosphate solutions at 250 ºC. These results demonstrated a two-stage replacement mechanism, and showed that an ultra-local equilibrium can form complex chemical zoning patterns in the partially reacted apatite, even when the overall system is highly fluid-buffered.

4.2. As(III) incorporation by apatite

Apatite synthesized from solutions spiked only with As(III) contained only As(III), with lower As concentrations than in the As(V)-bearing apatite for similar aqueous As concentrations (Fig. 2). EXAFS data indicate an arsenite-like structure (three-coordinated AsO_3^{3-} moiety with a stereochemically active electron lone pair), but with As-O bond distances of ~1.68-1.70 Å that are similar to As-O distances in the rigid arsenate group (~1.68 Å) but shorter than typical As(III)-O distances in crystals (1.77(3) Å; Ramirez-Solis et al. 2004) or in aqueous complexes (1.75-1.77(1) Å, Testemale et al. 2004). The short As(III)-O bond distances in our apatite indicate strong over-

412 bonding, i.e. 3.72 to 4.02 bond valence charges according to the parameters of Brown and
413 Altermatt (1985).

414 The threefold AsO_3^{3-} structure in apatite has been confirmed by *ab initio* molecular
415 simulations, which show the trigonal pyramidal geometry with the lone electron pair on top of
416 As(III) (Fig. 7b). For As(III) in apatite, the optimized distances are 1.74-1.76 Å, which are ~0.04 Å
417 longer than the distances determined from EXAFS fitting (1.69-1.70 Å). Slightly longer bond
418 distances from DFT-based simulations than experimental values are considered within typical
419 accuracy of such simulations (see Bühl and Kabrede (2006) for a discussion of the accuracy of
420 DFT calculations). For instances, the bond distance by DFT calculations are up to 0.05 and 0.07
421 Å longer than the experimental values for Mn-O and Pd-O distances (Tian et al., 2014; Mei et al.,
422 2015). Hence, the *ab initio* molecular simulations and the EXAFS data support the substitution of
423 arsenite moieties for phosphate groups in the apatite structure, although the short As-O bonds
424 indicate a strong local strain around the substituted positions. Considering the predominant species
425 in the experimental solutions at 250°C ($As(OH)_{3(aq)}$, $H_3PO_{4(aq)}$, and $H_2CO_{3(aq)}$, calculated using
426 HCh package), the replacement of calcite by As-bearing apatite in the presence of As(III)-bearing
427 solutions can be expressed as:

428 $$10CaCO_3(s) + (6-x)H_3PO_{4(aq)} + xAs(OH)_{3(aq)} + 2H_2O =$$
429 $$Ca_{10}(PO_4)_{6-x}(AsO_3)_x(OH)_2(s) + 10H_2CO_{3(aq)} \quad \textbf{(1)}$$

430 where x refers the moles of AsO3 moiety in the reaction product.

431 **4.3. Dynamic uptake of As(III) and As(V)**

432 For the mixed As(III)/As(V) experiments, both As(III) and As(V) can be substituted into
433 the apatite structure, and a complex distribution of As oxidation state was observed in the partially
434 reacted samples (Figs. 4, 5). We show that **(i)** the local equilibrium determines the heterogeneity
435 of the As(III)/As(V) distribution in the partially-reacted samples: As(V) reaches further to the
436 reaction front and center of the grain, whereas As(III) is more concentrated on the rim of the grain;
437 and **(ii)** As(III) in apatite is easily replaced by As(V) during progressive recrystallization of apatite.

438 As shown by the higher $As_{solid}/As_{solution}$ ratio for As(V) versus As(III) solutions (Fig. 2) and
439 the highly overbonded state of As(III) substituting for phosphate in the apatite structure (EXAFS
440 & DFT), it is easier for $As(V)O_4^{3-}$ to substitute for a phosphate group than $As(III)O_3^{3-}$. The low
441 affinity of the apatite crystal structure for As(III) is easily explained by the longer As(III)-O

442 distance compared to P-O, as well as by a stereochemical component (symmetrical tetrahedron
443 versus trigonal pyramid + lone pair).

444 Preferential uptake of As(V) versus As(III) results in a rapidly increasing As(III)/As(V)
445 ratio in the solution near the reaction front, assuming that apatite formation is faster than
446 As(III)/As(V) diffusion from the bulk of the solution to the reaction front. At the initiation of the
447 replacement reaction, aqueous phosphate, arsenate, and arsenite groups are in contact with the
448 calcite grains; as the reaction progresses, these moieties need to diffuse through an increasingly
449 thick layer of arsenian apatite to reach the reaction front. Phosphate and arsenate will diffuse at
450 similar rates (similar charges and geometries; $H_2AsO_4^-$ versus $H_2PO_4^-$ at 250 ˚C and near-neutral
451 pH; James-Smith et al. 2010; Shock and Helgeson 1988), whereas As(III) (as the neutral
452 $As(OH)_3(aq)$ complex; Testemale et al. 2004) differs by both its coordination geometry and its
453 neutral charge. One explanation for the observed zoning in the partially reacted samples is that
454 initially, there is a strong depletion of the As(V) in the fluid at the calcite surface/near the
455 replacement front, due to preferential uptake of As(V). This results in As(III) uptake into the
456 apatite structure. Somehow as reaction progresses, less As(III) is incorporated into the newly
457 formed apatite, which can reflect different transport properties of As(V)/As(III) in the porous
458 apatite, or a change in reaction mechanism that favors preferential formation of the lower energy
459 form of As-apatite.

460 In the fully replaced grains, after 48 hours all arsenite (AsO_3^{3-}) has been replaced by
461 arsenate (AsO_4^{3-}). This suggests that some extent of dynamic recrystallization took place in the
462 grains, that overprints the original As zoning. A similar two-steps reaction mechanism was
463 described by Borg et al. (2014) for the As(V) system, whereby a highly inhomogeneous and locally
464 As-rich apatite quickly recrystallized into a homogenous As-bearing apatite. In the As(V) only
465 case, recrystallization was driven by chemical gradients and the metastability of high-As apatite
466 with respect to the local solution compositions. In the case of apatite in mixed As(III)/(V)
467 solutions, recrystallization is probably driven by the high energy state (high strain) of the crystal
468 lattice around the As(III) ions. This process obliterates the dynamic uptake of As(III), provided
469 that As(V) ions are available in solution, and results in a final product that contains predominantly
470 As(V). Our experimental results show that although the existence of As(III) make the replacement
471 reaction less effective than As(V) system, indicated by total arsenic concentration (Fig. 2),
472 eventually As(V) is the predominant oxidation state in most As-rich apatite which has also been
473 seen in natural samples.

These results are consistent with recent studies on As(V) and As(III) incorporation into calcite, despite that apatite structure is a better than calcite for incorporating both As(V) and (III) due to similarity among PO_4^{3-}, AsO_4^{3-} and AsO_3^{3-} moieties. For example, for the natural calcite from As-bearing travertines in Italy, Benedetto et al. (2006) suggested that As(III) is present in the calcite structure via a $CO_3^{2-} \Leftrightarrow AsO_3^{3-}$ substitution, Bardelli et al. (2011) found mixed As(III) and As(V), and Costagliola et al. (2013) suggested 80% As(V) and 20% As(III) incorporation in these calcite. Yokoyama et al. (2012) showed experimentally that As(III) is incorporated into calcite only at high pH ($pH_{25^\circ C}$>=9.3), where anionic form As(III) species such as $H_2AsO_3^-$ predominate, and are able to interact with the calcite surface, contrary to the neutral $As(OH)_3$(aq). In Yokoyama et al. (2012)'s experiments, calcite incorporated only As(V) even in the systems spiked with As(III) at circum-neutral pH. They showed that As(III) was oxidized to As(V) as a result of the stabilization of As(V) in the presence of the Ca^{2+} ion, via the formation of thermodynamically stable complexes of As(V) with the Ca^{2+} ion in the calcite-supersaturated water. Renard et al. (2015) found As(III) is less incorporated in calcite than As(V), and partial oxidation of As(III) to As(V), with 36% As(III) and 64% As(V) in the reaction product. They confirmed the relatively small effect of $As(OH)_3$(aq) on calcite dissolution/growth by *in-situ* AFM, compared to charged complexes such as $H_2AsO_4^-$.

4.4. Consequences for trace element tracers

The natural As-bearing apatite from the Binntal gneiss and most As-bearing apatite from the Ernest Henry IOCG hydrothermal deposit contain predominantly As(V). We used the thermodynamic modeling package HCh (Shvarov, 2008) to estimate the oxidation state of As in the fluids from the observed mineral assemblages. For the Ernest Henry samples, the HCh calculations based on the assemblage of K-feldspar, muscovite, biotite, magnetite, and apatite (200-450 °C, 500-2500 bar, Cleverley and Oliver, 2005) shows that As(III) is the only oxidation state (e.g., 92% $As(OH)_3$(aq) and 8% $As_2SO_3^-$ at 300°C). For Binntal, the calculations assumed equilibrium with a metamorphic fluid, and similarly show that, even under oxidizing, hematite–magnetite buffered conditions, As(III) species are predominant (>99.9%, mainly as $As(OH)_3$(aq)) in the fluid at the T, P condition relevant to the formation of the apatite (~500 °C, 5,000 bar; note that pressure is limited by the equation of state used in HCh); therefore, it is unlikely that As(V) existed in the fluids from which these two apatites precipitated. Because As(III) uptake is controlled by dynamic processes (dependent on reaction mechanism) rather than equilibrium partitioning in apatite, apatite is not a reliable tracer for the fluid composition. However – and

rather surprisingly given the easy oxidation of As(III)-in-apatite during dynamic recrystallization observed in our experiments – As(III) can be retained in apatite over geological times. The As(V)-rich rim in Fig. 13 probably formed via replacement following a coupled-dissolution-reprecipitation mechanism of As(III) apatite; the As(V) apatite displays typical features for this type of reaction, including abundant micro-porosity, inclusions along the reaction front, and a sharp reaction front (Altree-Williams et al., 2015). Hence, the preservation of the As(III) in the core may be the result of armoring by an As(V) apatite in this particular grain.

In general, three possible processes may contribute to the scarcity of As(III) in most natural apatite samples, and selective incorporation of As(V).

1) Traces amounts of As(V) may have been present in the fluid, despite the suggestion from the thermodynamic modeling;

2) Apatite may have originally taken up As(III) from hydrothermal fluids, but this As(III) has since been oxidized to As(V), e.g. during recrystallization. This would mean that apatite intrinsically is not a good vehicle for preserving the original signature from the hydrothermal fluid. We note that XANES studies have demonstrated preservation of Eu^{2+} and Eu^{3+} in hydrothermal apatite (Rakovan et al. 2001; Takahashi et al. 2005). Together with the As(III) preserved in some Ernest Henry apatites, this shows that in some cases apatite can preserve oxidation state signatures over geological times;

3) Surface enhanced oxidation. The process of oxidation of As(III) via formation of stable As(V)-Ca complexes in the Ca-rich fluid layer near a dissolving calcite surface has been demonstrated at room-temperature by Yokoyama et al. (2012). A similar process could explain the uptake of As(V) from As(III)-dominated fluids by the measured natural apatites. Although such an effect was not observed in our As(III)-only experiments, it may happen under different conditions. Qian et al. (2013) observed a similar surface effect during the uptake of As by pyrite forming via the sulfidation of magnetite; no matter the oxidation state of the As-source, pyrite formed via this process contained predominantly As in an As(II)-like oxidation state.

Irrespective of the cause, As in apatite may not be able to record the original ratios of As oxidation states in the fluid, nor to preserve it during post-crystallization fluid-rock reactions. This example illustrates that one needs to exercise caution when interpreting chemical zonations in hydrothermal minerals (van Hinsberg et al. 2010). Overall, our experiments illustrate the role of local processes in the incorporation not only of trace elements in hydrothermal minerals, but also

their oxidation state. Brugger et al. (2008) found a complex zoning in Eu^{2+}/Eu^{3+} ratios preserved in hydrothermal scheelite, and interpreted it in terms of various degrees of fluid-rock reaction. In this case, an external control is supported by variation in Sr isotopic signature, which cannot be explained by chemical fractionation alone (Brugger et al. 2000, 2002). This illustrates the power and necessity of combining various approaches, e.g., trace element, oxidation state mapping, and isotopic studies to decipher the origin and significance of trace elements in minerals formed in the presence of fluids.

Our experimental and molecular simulation results indicate that As(III) can be substituted into PO_4^{3-} in terms of AsO_3^{3-}, which is similar to As(V) and As(III) incorporation into calcite structure shown in recent studies (e.g., Bardelli et al., 2011; Renard et al. 2015). Thus hydrothermal synthesis of apatite may provide a way to fix As(III), as well as As(V) from As-bearing aqueous fluids. However, the uptake and preservation of the As(III) in apatite are both controlled by kinetic processes (e.g., reaction pathway), and it is of paramount importance to take these aspects into consideration while designing geochemical barriers based on Ca-minerals for As(III/V) immobilization.

Acknowledgement: Research funding was provided by the Australian Research Council (ARC) to W. L. (FT130100510) and J.B. (DP140102765), and CSIRO OCE fellowship to Y.M. This research is also supported by the Science and Industry Endowment Fund. The bulk XAS data and the micro-XANES images were collected at the XAS and the XFM beamlines of the Australian Synchrotron, and quick-XANES imaging was carried out at the P06 beamline of the light source PETRA III at DESY, a member of the Helmholtz Association (HGF). The DFT calculations in this work were supported by resources provided by the Pawsey Supercomputing Centre with funding from the Australian Government and the Government of Western Australia. We thank the BCC group (Stéphane Cuchet, Mischa Crumbach, Ate van der Burgt) for providing the sample from Binntal. C.G.R acknowledges travel funding provided by the International Synchrotron Access Program (ISAP) managed by the Australian Synchrotron. The authors are grateful for the helpful reviews from Professor E. Ripley, Dr S. Rowins and an anonymous GCA reviewer.

5. References

Alam, M.S., Wu, Y., and Cheng, T. (2014) Silicate Minerals as a Source of Arsenic Contamination in Groundwater. Water Air and Soil Pollution, 225:2201.

Altree-Williams, A.L., Pring, A., Ngothai, Y. and Brugger, J. (2015) Textural and compositional complexities resulting from coupled dissolution-reprecipitation reactions in geomaterials. *Earth-Science Reviews*, 150, 628–651.

Ballirano, P. and Maras, A. (2002) Refinement of the crystal structure of arsenolite, As_2O_3, Zeitschrift für Kristallographie - New Crystal Structures, p. 177.

Bardelli, F., Benvenuti, M., Costagliola, P., Di Benedetto, F., Lattanzi, P., Meneghini, C., Romanelli, M. and Valenzano, L. (2011) Arsenic uptake by natural calcite: An XAS study. Geochimica et Cosmochimica Acta 75, 3011-3023.

Bath, A.B., Walshe, J.L., Cloutier, J., Verrall, M., Cleverley, J.S., Pownceby, M.I., Macrae, C.M., Wilson, N.C., Tunjic, J., Nortje, G.S., and Robinson, P. (2013) Biotite and Apatite as Tools for Tracking Pathways of Oxidized Fluids in the Archean East Repulse Gold Deposit, Australia. Economic Geology, 108, 667-690.

Becke A. D. (1988) Density-functional exchange-energy approximation with correct asymptotic behavior. Phys. Rev. A 38, 3098.

Borg S, Liu W, Pearce M, Cleverley J, MacRae C. (2014) Complex mineral zoning patterns caused by ultra-local equilibrium at reaction interfaces. Geology 42, 415-418.

Bothe, J.V. and Brown, P.W. (1999) Arsenic immobilization by calcium arsenate formation. Environmental Science & Technology 33, 3806-3811.

Brown, I.D., and Altermatt, D. (1985) Bond-valence parameters obtained from a systematic analysis of the inorganic crystal structure database. Acta Crystallographica, B41, 244-248.

Brugger J., Etschmann B., Pownsby M., Liu W., Grundler P., Brewe D. (2008) Oxidation state of europium in scheelite: Tracking fluid-rock interaction in gold deposits. Chemical Geology 257, 26-33.

Brugger, J. and Gieré, R. (1999) As, Sb, and Ce enrichment in minerals from a metamorphic Fe-Mn deposit (Val Ferrera, Eastern Swiss Alps). Canadian Mineralogist, 37, 37-52.

595 Brugger, J., Lahaye, Y., Costa, S., Lambert, D. (2000): Inhomogeneous distribution of REE in
596 scheelite and dynamics of Archaean hydrothermal systems (Mt Charlotte and Drysdale
597 gold deposits, Western Australia). *Contributions to Mineralogy and Petrology*, 139, 251-
598 264.

599 Brugger J., Maas R., Lahaye Y., McRae C., Ghaderi M., Costa S., Lambert D., Bateman R., and
600 Prince K. (2002): Origins of Nd-Sr-Pb isotopic variations in single scheelite grains from
601 Archaean gold deposits, Western Australia. Chemical Geology, 182, 203-225.

602 Bühl, M. and Kabrede, H., (2006) Geometries of transition-metal complexes from density
603 functional theory. Journal of Chemical Theory Computation 2, 1282–1290.

604 Car R. and Parrinello M. (1985) Unified approach for molecular dynamics and density-functional
605 theory. Phys. Rev. Lett. 55, 2471–2474.

606 Carrupt, E. (2003) New stratigraphic structural and geochemical data from Val Formazza - Binntal
607 area (Central Alps). Mémoires de Géologie, vol. 41. Imprimerie Chabloz S.A., Lausanne,
608 Switzerland. 118 pp.

609 Catti, M. and Ivaldi, G. (1983) On the topotactic dehydration $Ca_3(AsO_4)_2•11H_2O$ (phaunouxite) -
610 -> $Ca_3(AsO_4)_2•10H_2O$ (rauenthalite), and the structures of both minerals. Acta
611 Crystallographica Section B 39, 4-10.

612 Choong, T.S.Y., Chuah, T.G., Robiah, Y., Gregory Koay, F.L. and Azni, I. (2007) Arsenic toxicity,
613 health hazards and removal techniques from water: an overview. Desalination 217, 139-
614 166.

615 Cleverley, J.S. and Oliver, N.H.S. (2005) Comparing closed system, flow-through and fluid
616 infiltration geochemical modelling: examples from K-alteration in the Ernest Henry Fe-
617 oxide–Cu–Au system. Geofluids 5, 289-307.

618 Costagliola, P., Bardelli, F., Benvenuti, M., Di Benedetto, F., Lattanzi, P., Romanelli, M., Paolieri,
619 M., Rimondi, V. and Vaggelli, G. (2013) Arsenic-bearing calcite in natural travertines:
620 Evidence from sequential extraction, μXAS, and μXRF. Environmental Science and
621 Technology 47, 6231-6238.

622 Cuchet, S., Crumbach, M., van der Burgt, A. (2014) The Binntal reveals a big secret (in German
623 and French). Schweizer Strahler, 2/2014, 2-55.

624 Etschmann, B.E., Donner, E., Brugger, J., Howard, D.L., de Jonge, M.D., Paterson, D., Naidu, R.,
625 Scheckel, K.G., Ryan, C.G., and Lombi, E. (2014) Speciation mapping of environmental
626 samples using XANES imaging. Environmental Chemistry, 11, 341-350.

627 Etschmann, B., Ryan, C., Brugger, J., Kirkham, R., Hough, R., Moorhead, G., Siddons, D., De
628 Geronimo, G., Kuczewski, A., Dunn, P., Paterson, D., de Jonge, M., Howard, D., Davey,
629 P., and Jensen, M. (2010) Reduced As components in highly oxidized environments:
630 Evidence from full spectral XANES imaging using the Maia massively parallel detector.
631 American Mineralogist, 95, 884-887.

632 Ferraris, G., and Chiari, G. (1970) Crystal structure of $Na_2HAsO_4.7H_2O$. Acta Crystallographica
633 Section B-Structural Crystallography and Crystal Chemistry, B 26, 1574-1583.

634 Gregory C., Rubatto D., Hermann J., Berger A. & Engi M. (2012) Allanite behaviour during
635 incipient melting in the southern Central Alps. Geochimica et Cosmochimica Acta 84, 433-
636 458.

637 Harlov D.E., (2015) Apatite: A Fingerprint for Metasomatic Processes. Elements 11, 171-176.

638 Hughes, J.M. and Rakovan, J.F. (2015) Structurally Robust, Chemically Diverse: Apatite and
639 Apatite Supergroup Minerals. Elements 11, 165-170.

640 James-Smith, J., Cauzid, J., Testemale, D., Liu, W., Hazemann, J., Proux, O., Etschmann, B.,
641 Philippot, P., Banks, D., Williams, P., Brugger, J. (2010) Arsenic speciation in fluid
642 inclusions using micro-beam X-ray absorption spectroscopy. American Mineralogist 95,
643 921-932.

644 Jamieson, H.E., Walker, S.R., Andrade, C.F., Wrye, L.A., Rasmussen, P.E., Lanzirotti, A., and
645 Parsons, M.B. (2011) Identification and Characterization of Arsenic and Metal Compounds
646 in Contaminated Soil, Mine Tailings, and House Dust Using Synchrotron-Based
647 Microanalysis. Human and Ecological Risk Assessment, 17, 1292-1309.

648 Jolly, W. L. (1984) Modern Inorganic Chemistry. McGraw-Hill. p. 77–90.

649 Kasioptas, A., Geisler, T., Perdikouri, C., Trepmann, C., Gussone, N. and Putnis, A. (2011)
650 Polycrystalline apatite synthesized by hydrothermal replacement of calcium carbonates.
651 Geochimica et Cosmochimica Acta 75, 3486-3500.

652 Kirkham R., Dunn P.A., Kucziewski A., Siddons D.P., Dodanwela R., Moorhead G., Ryan C.G.,
653 De Geronimo G., Beuttenmuller R., Pinelli D., Pfeffer M., Davey P., Jensen M., Paterson

D., de Jonge M.D., Kusel M. and McKinlay J. (2010) The Maia Spectroscopy Detector System: Engineering For Integrated Pulse Capture, Low-Latency Scanning And Real-Time Processing. AIP Conference series, 1234, 240-243.

Knill, M.D. (1996) The Pb-Zn-As-Tl-Ba-deposit at Lendenbach, Binn Valley, Switzerland. Beiträge zur Geologie der Schweiz, Geotechnische Serie, 90, 74 pp.

Lee, Y.J., Stephens, P.W., Tang, Y., Li, W., Phillips, B.L., Parise, J.B. and Reeder, R.J. (2009) Arsenate substitution in hydroxylapatite: Structural characterization of the $Ca_5(P_xAs_{1-x}O_4)_3OH$ solid solution. American Mineralogist 94, 666-675.

Lee C., Yang W. and Parr R. G. (1988) Development of the Colle-Salvetti correlation-energy formula into a functional of the electron density. Phys. Rev. B 37, 785.

Li, K., Etschmann, B.E., Rae, N., Reith, F., Ryan, C.G., Kirkham, R., Howard, D., Rosa, D., Zammit, C. Pring, A., Ngothai, Y., Hooker, A. and Brugger, J. (2016) Ore petrography using megapixel X-ray imaging: Rapid insights into element distribution and mobilisation in complex Pt and U-Ge-Cu ores. Economic Geology, 111, 487-501.

Mao, M., Rukhlov, A.S., Rowins, S.M., Spence, J. and Coogan, L.A. (2016) Apatite Trace Element Compositions: A Robust New Tool for Mineral Exploration. Economic Geology 111, 1187-1222.

Mei, Y., Etschmann, B., Liu, W., Sherman, D.M., Barnes, S.J., Fiorentini, M.L., Seward, T.M., Testemale, D. and Brugger, J. (2015) Palladium complexation in chloride- and bisulfide-rich fluids: Insights from ab initio molecular dynamics simulations and X-ray absorption spectroscopy. Geochimica Et Cosmochimica Acta 161, 128-145.

Pan, Y.M. and Fleet, M.E. (2002) Compositions of the apatite-group minerals: Substitution mechanisms and controlling factors. Rev Mineral Geochem 48, 13-49.

Pasero, M., Kampf, A. R., Ferraris, C., Pekov, I. V., Rakovan, J. and White, T. J. (2010) Nomenclature of the apatite supergroup minerals. European Journal of Mineralogy 22, 163-179.

Paterson, D., de Jonge, M. D., Howard, D. L., Lewis, W., McKinlay, J., Starritt, A., Kusel, M., Ryan, C. G., Kirkham, R., Moorhead, G., and Siddons, D. P. (2011) The X-ray Fluorescence Microscopy Beamline at the Australian Synchrotron. AIP Conf. Proc. 1365, 219-222.

684 Putnis, A. (2009) Mineral Replacement Reactions. Reviews in Mineralogy and Geochemistry 70,
685 87-124.

686 Qian, G., Brugger, J., Testemale, D., Skinner, W., and Pring, A. (2013) Formation of As(II)-pyrite
687 during experimental replacement of magnetite under hydrothermal conditions. Geochimica
688 Et Cosmochimica Acta, 100, 1-10.

689 Rakovan, J., Newville, M., Sutton, S. (2001) Evidence of heterovalent europium in zoned
690 Llallagua apatite using wavelength dispersive XANES. Am. Mineral. 86, 697–700.

691 Ramirez-Solis, A., Mukopadhyay, R., Rosen, B.P., and Stemmler, T.L. (2004) Experimental and
692 theoretical characterization of arsenite in water: Insights into the coordination environment
693 of As-O. Inorganic Chemistry, 43(9), 2954-2959.

694 Renard, F., Putnis, C.V., Montes-Hernandez, G., Ruiz-Agudo, E., Hovelmann, J. and Sarret, G.
695 (2015) Interactions of arsenic with calcite surfaces revealed by in situ nanoscale imaging.
696 Geochimica et Cosmochimica Acta 159, 61-79.

697 Rusk, B., Oliver, N., Cleverley, J., Blenkinsop, T., Zhang, D., Williams, P. and Habermann, P.
698 (2010) Physical and chemical characteristics of the Ernest Henry iron oxide copper gold
699 deposit, Australia; implications for IOGC genesis. In: Porter, T.M., (ed.) Hydrothermal
700 Iron Oxide Copper-Gold & Related Deposits: a global perspective - advances in the
701 understanding of IOCG deposits. Global Perspective Series, 3. PGC Publishing, Linden
702 Park, SA, Australia, pp. 201-218.

703 Ryan C.G., Cousens D.R., Sie S.H., Griffin W.L., Suter G.F. and Clayton E. (1990) Quantitative
704 PIXE Microanalysis of Geological Material using the CSIRO Proton Microprob. Nucl.
705 Instr. and Meth. B47, 55-72.

706 Ryan C.G. and Jamieson D.N. (1993) Dynamic Analysis: On-line Quantitative PIXE
707 Microanalysis and its Use in Overlap-Resolved Elemental Mapping. Nucl. Instr. and Meth.
708 B77, 203-214.

709 Ryan C.G. (2000) Quantitative Trace Element Imaging using PIXE and the Nuclear Microprobe",
710 International Journal of Imaging Systems and Technology, Special issue on "Advances in
711 Quantitative Image Analysis. 11, 219-230.

712 Ryan C.G., Siddons D.P., Kirkham R., Dunn P.A., Kuczewski A., Moorhead G., De Geronimo G.,
713 Paterson D.J., de Jonge M.D., Hough R.M., Lintern M.J., Howard D.L., Kappen P. and

714 Cleverley J. (2010a) The New Maia Detector System: Methods for High Definition Trace
715 Element Imaging of Natural Material. X-Ray Optics and Microanalysis, AIP Conference
716 Proc. 1221, 9-17; doi:10.1063/1.3399266.

717 Ryan C.G., Kirkham R., Hough R.M., Moorhead G., Siddons D.P., de Jonge M.D., Paterson D.J.,
718 De Geronimo G., Howard D.L. and Cleverley J.S. (2010b) Elemental X-ray imaging using
719 the Maia detector array: The benefits and challenges of large solid-angle. Nucl. Instr. Meth
720 A 619, 37-43 (DOI: 10.1016/j.nima.2009.11.035).

721 Ryan, C.G., Siddons, D.P., Kirkham, R., Li, Z.Y., de Jonge, M.D., Paterson, D.J., Kuczewski, A.,
722 Howard, D.L., Dunn, P.A., Falkenberg, G., Boesenberg, U., De Geronimo, G., Fisher, L.A.,
723 Halfpenny, A., Lintern, M.J., Lombi, E., Dyl, K.A., Jensen, M., Moorhead, G.F., Cleverley,
724 J.S., Hough, R.M., Godel, B., Barnes, S.J., James, S.A., Spiers, K.M., Alfeld, M.,
725 Wellenreuther, G., Vukmanovic, Z. and Borg, S. (2014) Maia X-ray fluorescence imaging:
726 Capturing detail in complex natural samples. J Phys Conf Ser 499.

727 Schroer, C. G., Boye, P., Feldkamp, J. M., Patommel, J., Samberg, D., Schropp, A., Schwab, A.,
728 Stephan, S., Falkenberg, G., Wellenreuther, G., et al. (2010). Nucl. Instruments Methods
729 Phys. Res. Sect. A Accel. Spectrometers, Detect. Assoc. Equip. 616, 93–97.

730 Shock, E.L., and Helgeson, H.C. (1988) Calculation of the thermodynamic and transport properties
731 of aqueous species at high pressures and temperatures: Correlation algorithms for ionic
732 species and equation of state predictions to 5kb and 1000˚C. Geochim. Cosmochim. Acta,
733 52, 2009-2036.

734 Shannon, R.D. (1976) Revised effective ionic radii and systematic studies of interatomic distances
735 in halides and chalcogenides. Acta Crystallographica, A32, 751-767.

736 Shvarov, Y.V. (2008) HCh: New potentialities for the thermodynamic simulation of geochemical
737 systems offered by windows. Geochemistry International 46, 834-839.

738 Slepko, A., and Demkov, A.A. (2011) First-principles study of the biomineral hydroxyapatite.
739 Physical Review B, 84(13).

740 Smith, P.G., Koch, I., Gordon, R.A., Mandoli, D.F., Chapman, B.D., Reimer, K.J. (2005) X-ray
741 Absorption Near-Edge Structure Analysis of Arsenic Species for Application to Biological
742 Environmental Samples. Environmental Science & Technology 39, 248-254.

743 Takahashi, Y., Kolonin, G.R., Shironosova, G.P., Kupriyanova, I.I., Uruga, T., Shimizu, H. (2005)
744 Determination of the Eu(II)/Eu(III) ratios in minerals by X-ray absorption near-edge
745 structure (XANES) and its application to hydrothermal deposits. Mineral. Mag. 69, 179–
746 190.

747 Terra, J., Dourado, E.R., Eon, J.G., Ellis, D.E., Gonzalez, G., and Rossi, A.M. (2009) The structure
748 of strontium-doped hydroxyapatite: an experimental and theoretical study. Phys Chem
749 Chem Phys, 11(3), 568-77.

750 Testemale, D., Hazemann, J.L., Pokrovski, G.S., Joly, Y., Roux, J., Argoud, R. and Geaymond, O.
751 (2004) Structural and electronic evolution of the $As(OH)_3$ molecule in high temperature
752 aqueous solutions: An x-ray absorption investigation. Journal of Chemical Physics 121,
753 8973-8982.

754 Tian, Y., Etschmann, B., Mei, Y., Grundler, P.V., Testemale, D., Hazemann, J.L., Elliott, P.,
755 Ngothai, Y. and Brugger, J. (2014) Speciation and thermodynamic properties of
756 manganese(II) chloride complexes in hydrothermal fluids: In situ XAS study. Geochimica
757 et Cosmochimica Acta 129, 77-95.

758 Troullier N. and Martins J. L. (1991) Efficient pseudopotentials for plane-wave calculations. Phys.
759 Rev. B 43, 1993.

760 van Hinsberg, V.J., Migdisov, A.A., and Williams-Jones, A.E. (2010) Reading the mineral record
761 of fluid composition from element partitioning. Geology, 38(9), 847-850.

762 White, T.J., and Dong, Z.L. (2003) Structural derivation and crystal chemistry of apatites. Acta
763 Crystallographica Section B-Structural Science Crystal Engineering and Materials, 59, 1-
764 16.

765 Wilson, R.M., Elliott, J.C. and Dowker, S.E.P. (1999) Rietveld refinement of the crystallographic
766 structure of human dental enamel apatites. American Mineralogist 84, 1406-1414.

767 Yokoyama, Y., Tanaka, K. and Takahashi, Y. (2012) Differences in the immobilization of arsenite
768 and arsenate by calcite. Geochimica et Cosmochimica Acta 91, 202-219.

769 Zeglinski, J., Nolan, M., Bredol, M., Schatte, A., and Tofail, S.A. (2012) Unravelling the specific
770 site preference in doping of calcium hydroxyapatite with strontium from ab initio
771 investigations and Rietveld analyses. Phys Chem Chem Phys, 14(10), 3435-43.

Zhang, X., Zhu, Y., Zeng, H., Wang, D., Liu, J., Liu, H., Qian, M. and Xu, L. (2011) Dissolution and solubility of the arsenate–phosphate hydroxylapatite solid solution [$Ca_5(P_xAs_{1-x}O_4)_3(OH)$] at 25°C. Environmental Chemistry 8, 133-145.

Zhu, Y., Zhang, X., Long, F., Liu, H., Qian, M. and He, N. (2009) Synthesis and characterization of arsenate/phosphate hydroxyapatite solid solution. Materials Letters 63, 1185-1188.

779 Tables

780 Table 1. Sample information for the experiments of calcite to apatite hydrothermal replacement at
781 250 ˚C. As(III)/As(V) is molar ratio.

Series name	Sample name	Starting composition	As(III)/As(V) content in initial solution	Reaction time (hours)	XAS measurement
Series V	V-2-8	Calcite + 1.4 m $(NH_4)_2HPO_4$ and 0.12 m Na_2HAsO_4 solutions	As(V) = 0.12 m	20	Bulk
Series III	III-9-6 III-13-5 III-13-8	Calcite + 1.3 m $(NH_4)_2HPO_4$ and 0.01 – 0.14 m As_2O_3	As(III) = 0.14 m As(III) = 0.03 m As(III) = 0.14 m	48 48 48	Bulk Bulk Bulk
Series M	M-5 M-6 M-7 M-8 M-9	Calcite + mixture of $(NH_4)_2HPO_4P$, Na_2HAsO_4 and As_2O_3 solutions	As(III)/As(V) = 0.2 As(III)/As(V) =1.0 As(III)/As(V) =1.0 As(III)/As(V) =10.5 As(III)/As(V) =10.5	48 48 3 48 3	Bulk micro + Bulk micro Bulk micro

782

783

784 Table 2. Results of EXAFS refinement for As_2O_3, Na_2HAsO_4 and AS-bearing apatite, fitted using both k^2
785 and k^3 weighting; S_0^2=0.88

Sample	XANES results	N	R_O [Å]	σ^2 [Å^2]	ΔE (eV)	Reduced χ^2	R factor	R range [Å]	K range [Å^{-1}]
As_2O_3	As(III)	3 (fixed)	1.805(4)	0.003	10.62	99	0.019	R1-5	2-14
Na_2HAsO_4	As(V)	4 (fixed)	1.697(7)	0.004	6.24	119	0.03	R1-3	2-13.5
III-13-5 As(III)	O Ca ms	2.6(2) 1 (fix) As-O-O-As	1.69(1) 3.19(4) 3.28(1)	0.006(1) 0.003 (fix) 0.006(1)	9(1)	225	0.01	0.8-3.8	2.5-10
III-9-6 As(III)	O Ca ms	2.4(2) 1 (fix) As-O-O-As	1.70 (1) 3.21(3) 3.32(8)	0.0058(9) 0.003 (fix) 0.0058(9)	11(1)	2169	0.01	0.8-3.8	2.5-10
M-5 As(V)	O Ca Ca	3.7(3) 1 (fix) 1 (fix)	1.68(1) 3.27(2) 3.67(5)	0.0017(8) 0.005(4) 0.005(4)	10(1)	595	0.03	0.8-3.8	2.5-13
M-8 As(V)	o Ca Ca	3.5(2) 1 (fix) 1(fix)	1.68(1) 3.27(2) 3.66(5)	0.001 (fix) 0.004(3) 0.004(3)	10(1)	1017	0.02	0.8-3.8	2.5-10

786

787

788

789 Table 3 Results of geometry optimization of As in apatite using ab initio molecular simulation, and
790 comparison of P-O and As-O bond lengths with some standard compound.

Crystal	Super-cell Formula	Calculated bond length [Å]		Experimental bond length [Å]	
		P-O	As-O	P-O	As-O
Arsenolite	$As_{32}O_{48}$		1.815		1.786[1], 1.805(4)*
hydroxylapatite	$Ca_{30}(PO_4)_{18}(OH)_6$	1.55-1.56		1.542[2]	
As(V)- hydroxylapatite	$Ca_{30}(PO_4)_{17}(AsO_4)(OH)_6$	1.55-1.56	1.68-1.69		1.68(1) *
As(III)-hydroxylapatite	$Ca_{30}(PO_4)_{17}(AsO_3)(OH)_6$	1.55-1.56	1.74-1.76		1.69-1.70*
$As(OH)_3$(aq)					1.76(1)[3]
Calcium-arsenate					1.685[4]

791 [1] Ballirano and Maras (2002); [2] Wilson et al. (1999); [3] Testemale et al. (2004); [4] Catti and Ivaldi
792 (1983); * EXAFS refinement in this study (Table 2).

793

794

795

796

797

Figure Captions:

Fig. 1. As K-edge XANES spectra of bulk measurement of two standards (As_2O_3 for As(III) and sodium arsenate for As(V)), one sample from As(V) solution (V-2-8), two samples from As (III) solutions (III-13-5 and III-13-8), and partially reacted apatite from mixed As(III)/As(V) solutions (M-5: As(III)/As(V) = 0.01; M-6: ratio = 1; M-8: Ratio = 10).

Fig. 2. Arsenic concentration in final hydroxylapatite product measured by inductively coupled plasma–optical emission spectrometry (ICP-OES) as function of initial arsenic content in hydrothermal solutions. The reaction time is 48 hours, the As(III) data are from this study and the As(V) data are from Borg et al. (2014).

Fig. 3. As k-edge XANES spectra (a) and X-ray fluorescence map (b) for Sample M-6 (48 hours, AS(III)/As(V) ratio = 1. The XANES spectra are extracted from areas highlighted in the box in (a).

Fig. 4. As k-edge XANES spectra (a) and X-ray fluorescence map (b) for sample M-7 (3 hours, As(III)/As(V) = 1 in fluid). The XANES spectra are extracted from areas highlighted in the box in (a).

Fig. 5. Arsenic distribution and oxidation state in the reaction rim of sample M-9 (3 hours, As(III)/As(V) in fluid = 10). Sub plots a-d are data collected at the XFM beamline of the Australian Synchrotron: As k-edge XANES spectra (a), $As(III)/As_{total}$ ratio (b) and X-ray fluorescence map (c). The mapped area is located at the top corner of the partially reacted calcite grain shown in (d); subplots (e) and (f) are data collected at P06 beamline of the PETRA synchrotron. The XANES spectra are extracted from the areas highlighted in the boxes in (a) and (d).

Fig. 6. Measured and fitted As K-edge EXAFS spectra (a) and Fourier transforms (b) for As(V) and As(III)-bearing apatites, and two standard compound of As_2O_3 and $Na_2HAsO_4(H_2O)_7$.

Figure 7. Optimized geometry and local electron density of (a) arsenolite (As_2O_3), showing lone electron pair near As(III); and (b) As(III) in replacing phosphate in apatite (configuration (a) in Figure 10.

Figure 8. Results from first-principle geometry optimisation for apatite (a) and As(V)-bearing apatite (b), compared to crystal structure of johnbaumite (c) measured by Lee et al. (2009).

Figure 9. Optimized geometry of As(III)-hydroxylapatite in four possible configurations for the oxygen vacancy.

Figure 10. Apatite from amphibolite facies quartz-K-feldspar-muscovite-biotite gneiss, Binntal Valley, Switzerland. **(a)** Extracted XANES spectrum; **(b)** X-ray fluorescence map. The XANES spectra are extracted from the area highlighted in the box of (a).

Figure 11. As-bearing apatite grain (EH4-9) from the Ernest Henry IOCG deposit, Queensland, Australia. **(a)** XANES spectra and **(b)** backscattered electron image and **(c)** X-ray fluorescence map of an apatite grain. The XANES spectra are extracted from the area numbered in (c).

Figure 12. As-bearing apatite from the Ernest Henry IOCG deposit, Queensland, Australia. The figure illustrates As distribution and speciation for a cluster of apatite grains. **(a)** XANES spectra and **(b)** backscattered electron image and **(c)** X-ray fluorescence map of a cluster of grain EH545. The XANES spectra are extracted from the area highlighted in the box of (a), showing that only one grain has As(III) feature in the core.

Figure 13. As-bearing apatite (EH5452-6) from the Ernest Henry IOCG deposit, Queensland, Australia. **(a)** XANES spectra and **(b)** SEM image (BSE mode) and **(c)** X-ray fluorescence map of grain EH545. The XANES spectra are extracted from the area highlighted in the box of (a).

Figure 1

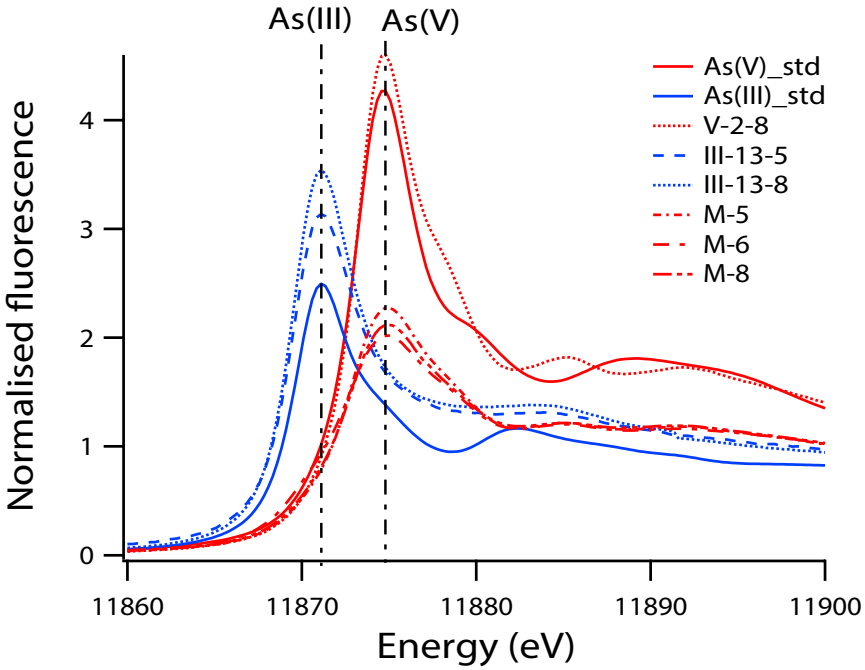

Fig 1

Figure 2

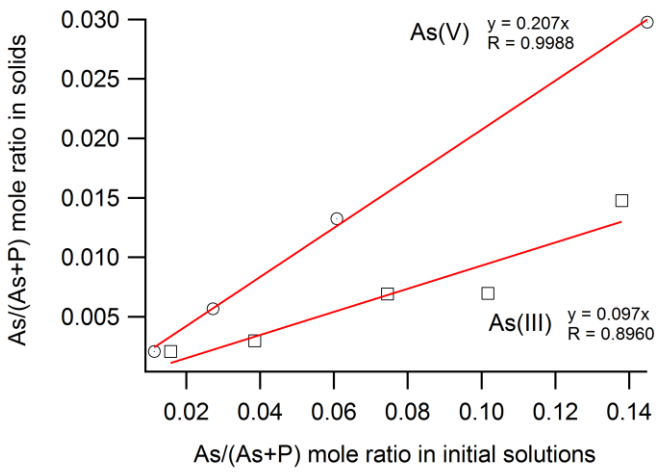

Fig 2

Figure 3

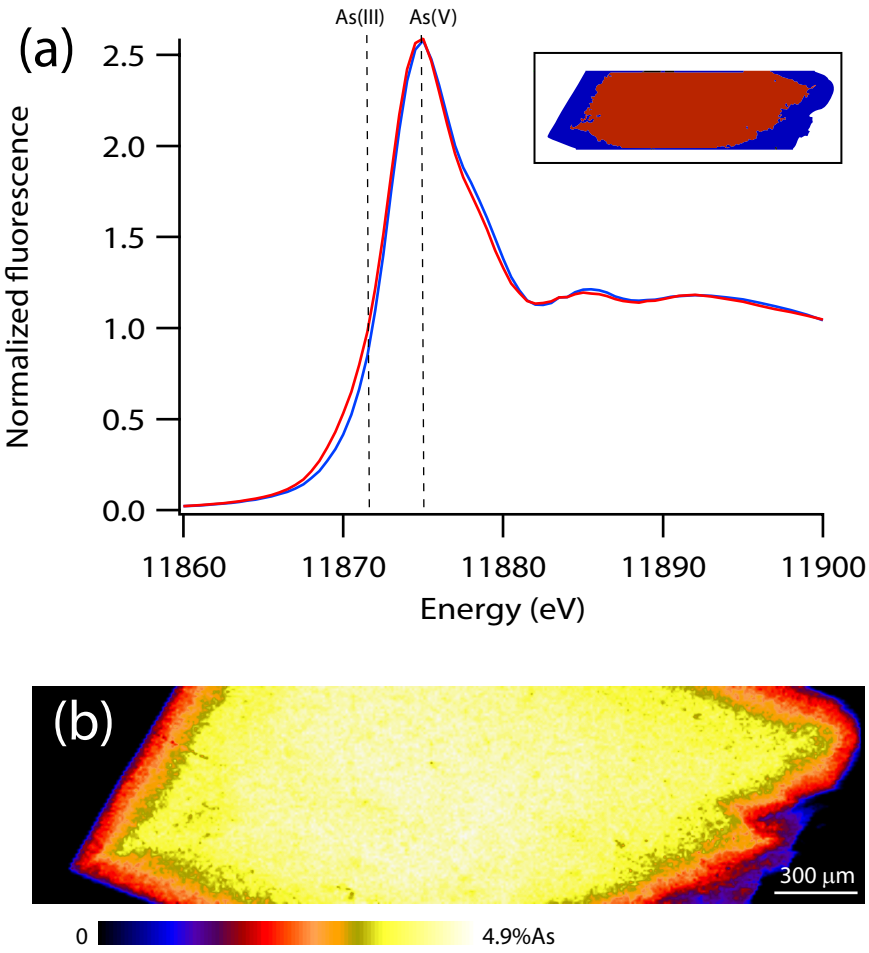

Fig. 3

Figure 4

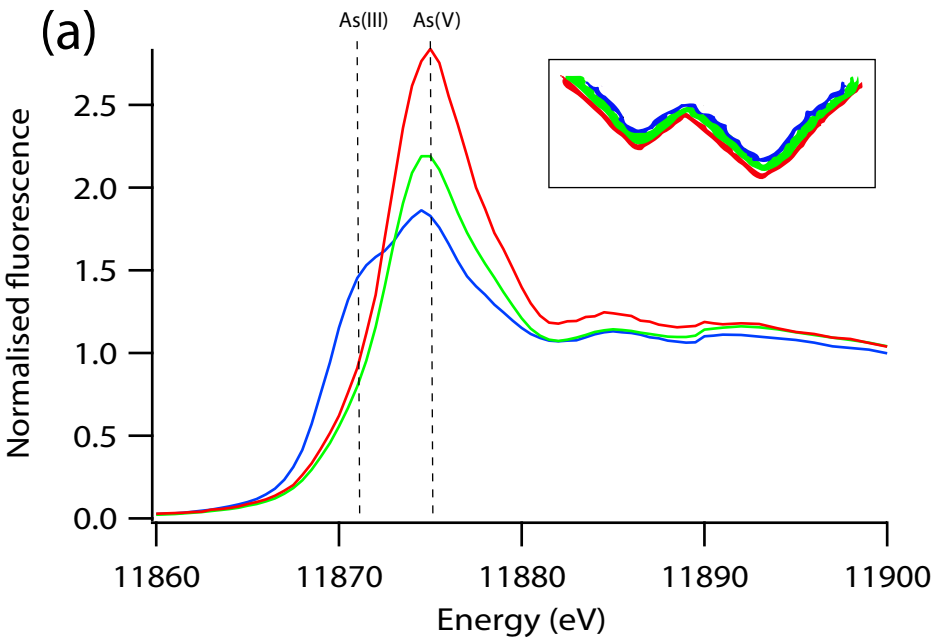

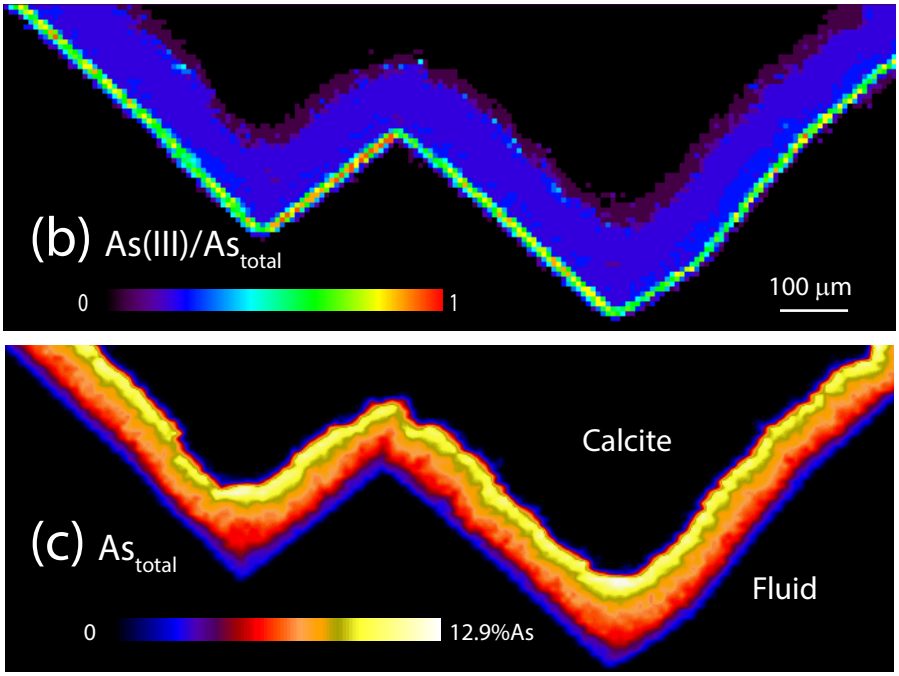

Fig 4

Figure 5

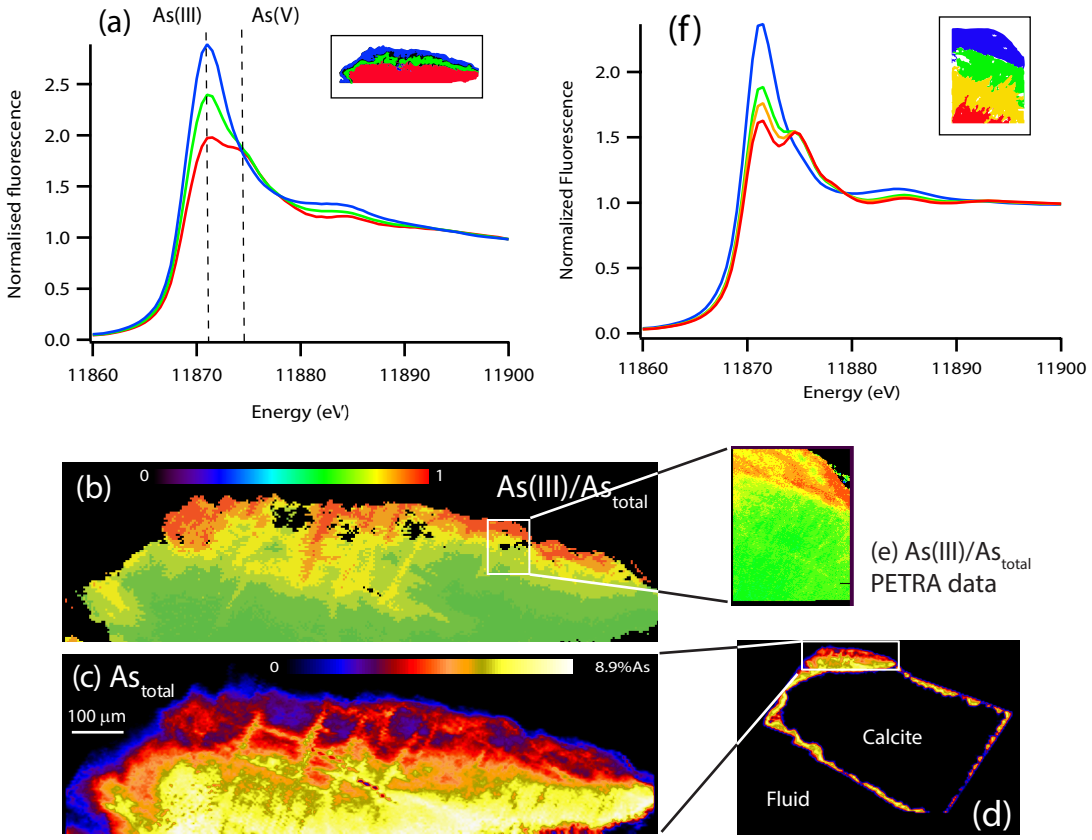

Fig 5

Figure 6

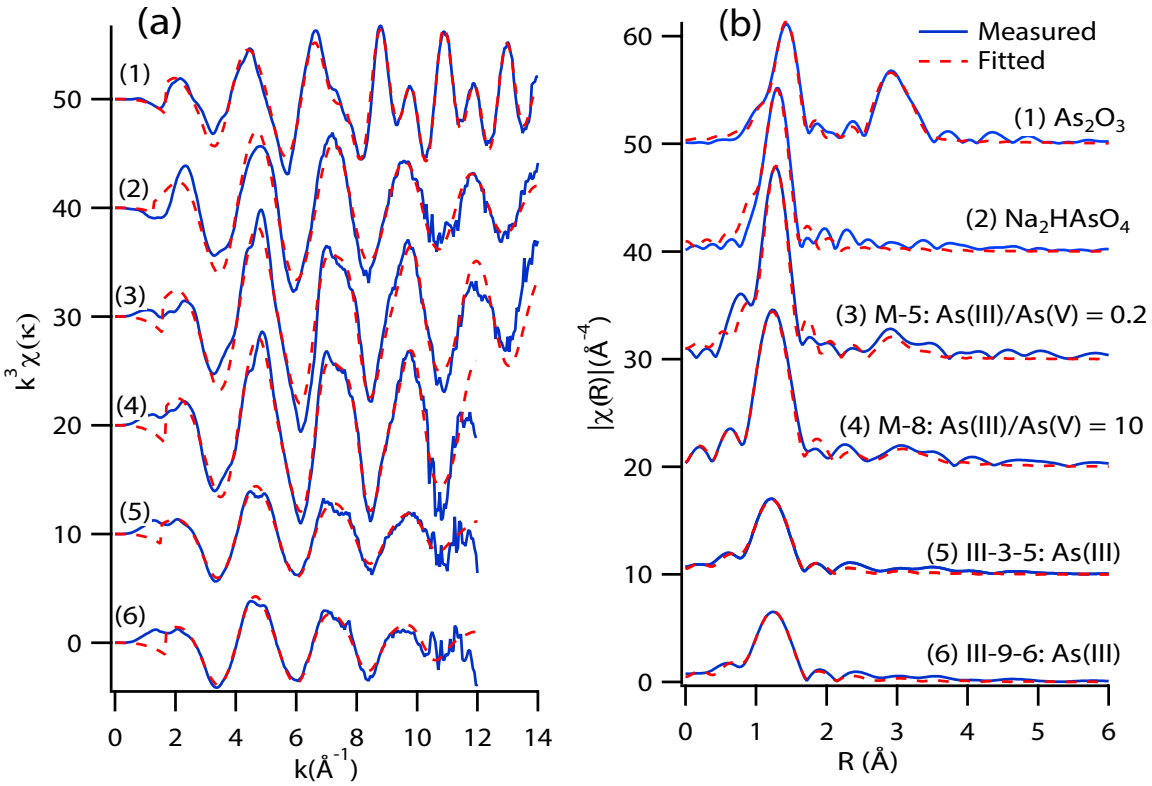

Fig 6

Figure 7

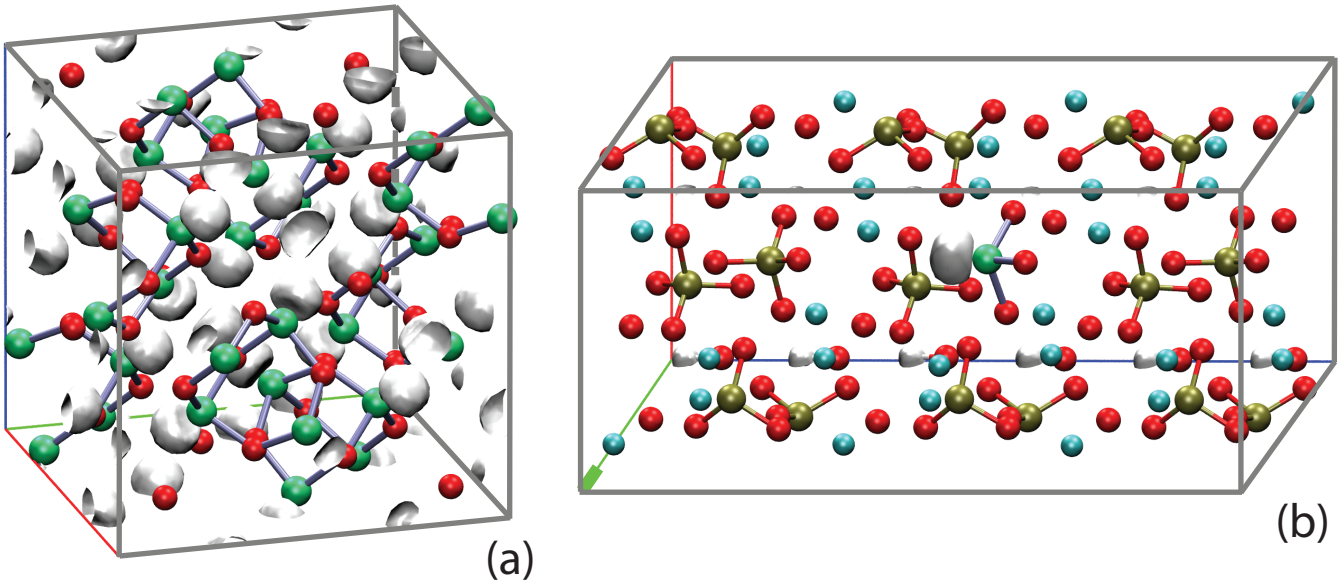

Fig 7

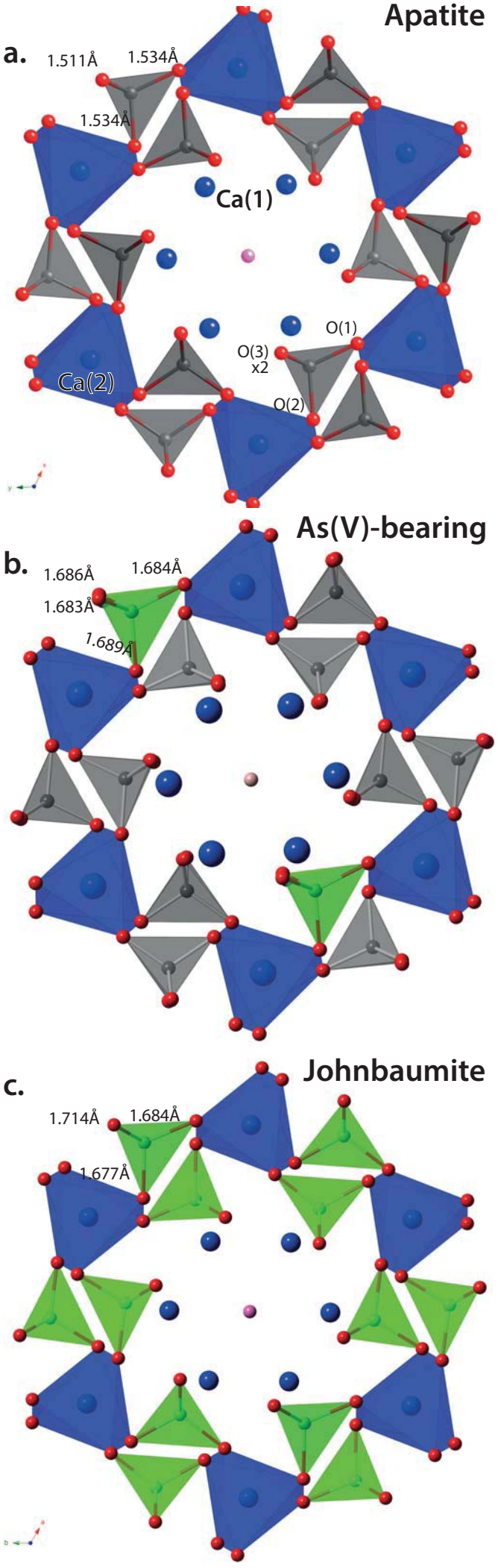
a.
Apatite
1.511Å
1.534Å
1.534Å
Ca(1)
O(1)
O(3)
x2
Ca(2)
O(2)
b.
As(V)-bearing
1.686Å
1.684Å
1.683Å
1.689Å
c.
Johnbaumite
1.714Å
1.684Å
1.677Å

Fig 8

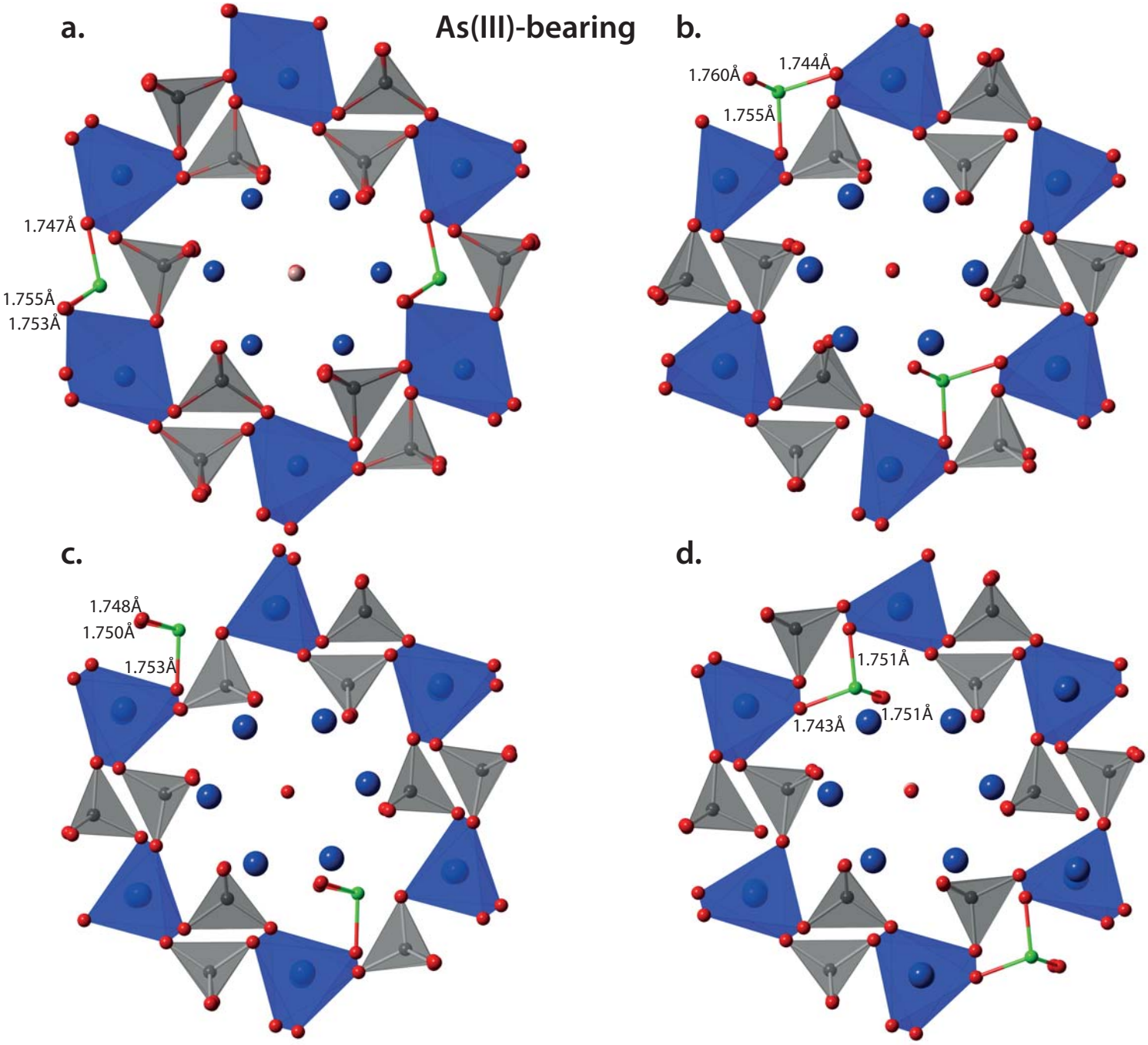
a.
As(III)-bearing
1.747Å
1.755Å
1.753Å
b.
1.760Å
1.744Å
1.755Å
c.
1.748Å
1.750Å
1.753Å
d.
1.751Å
1.743Å
1.751Å

Fig 9

Figure 10

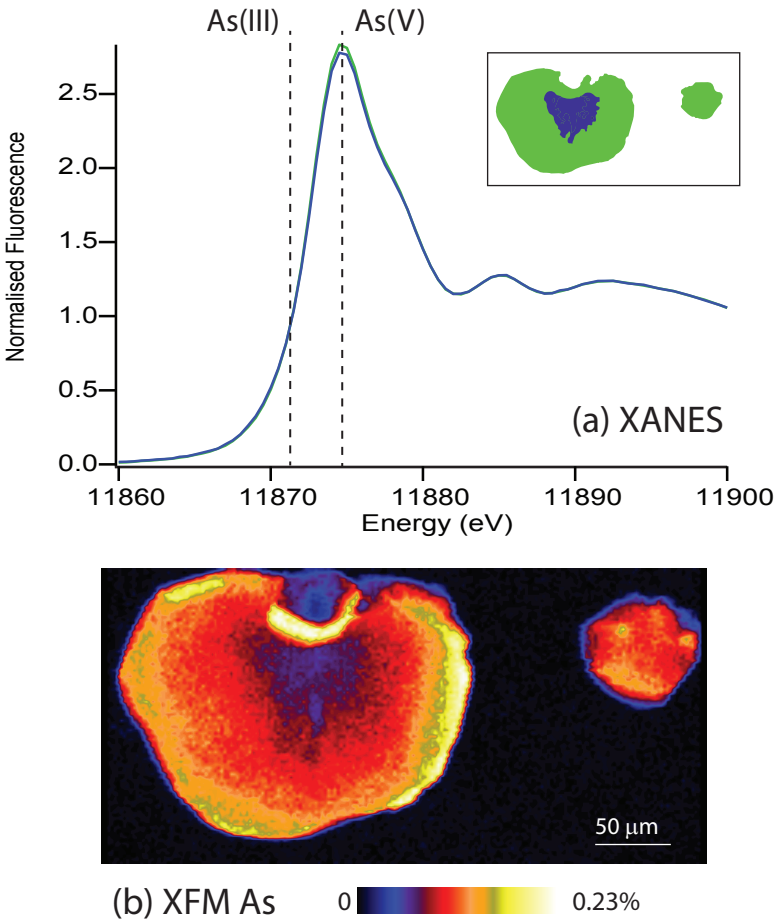

Fig. 10

Figure 11

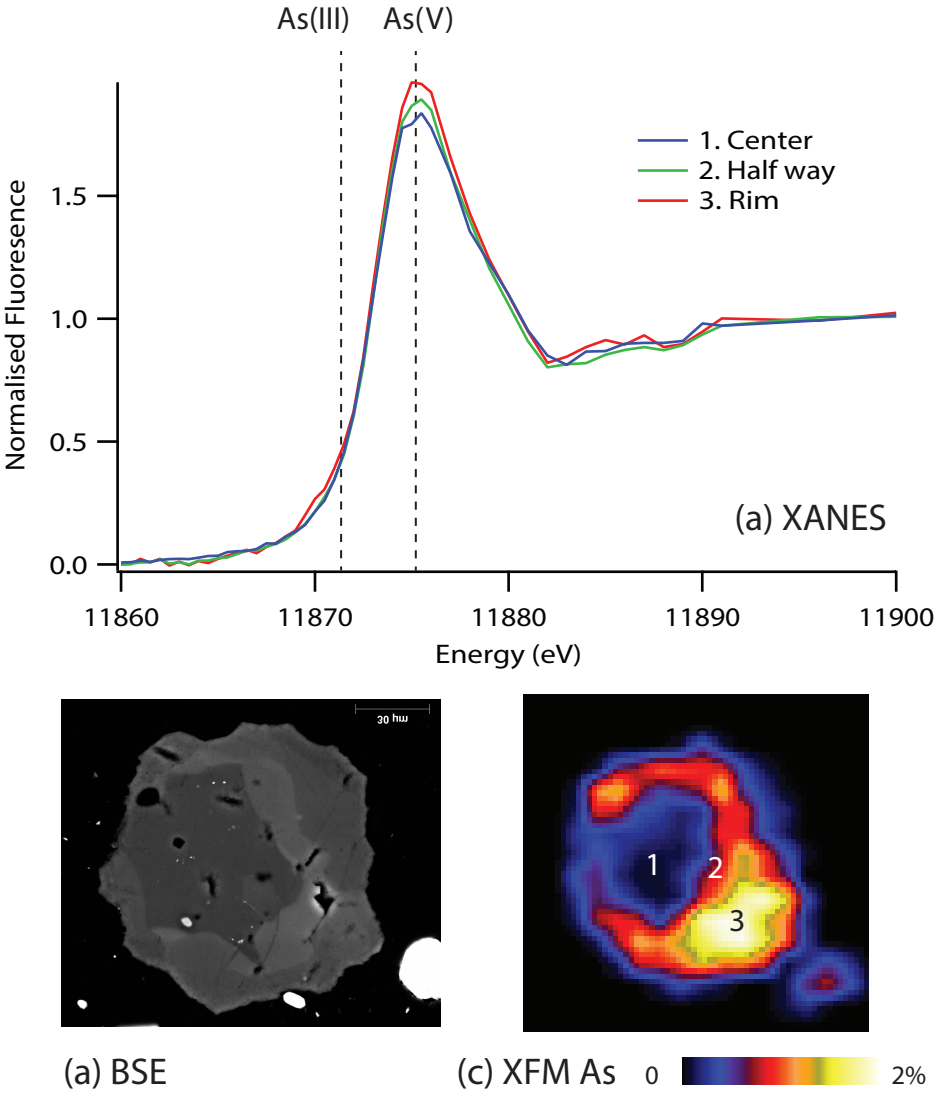

Fig. 11

Figure 12

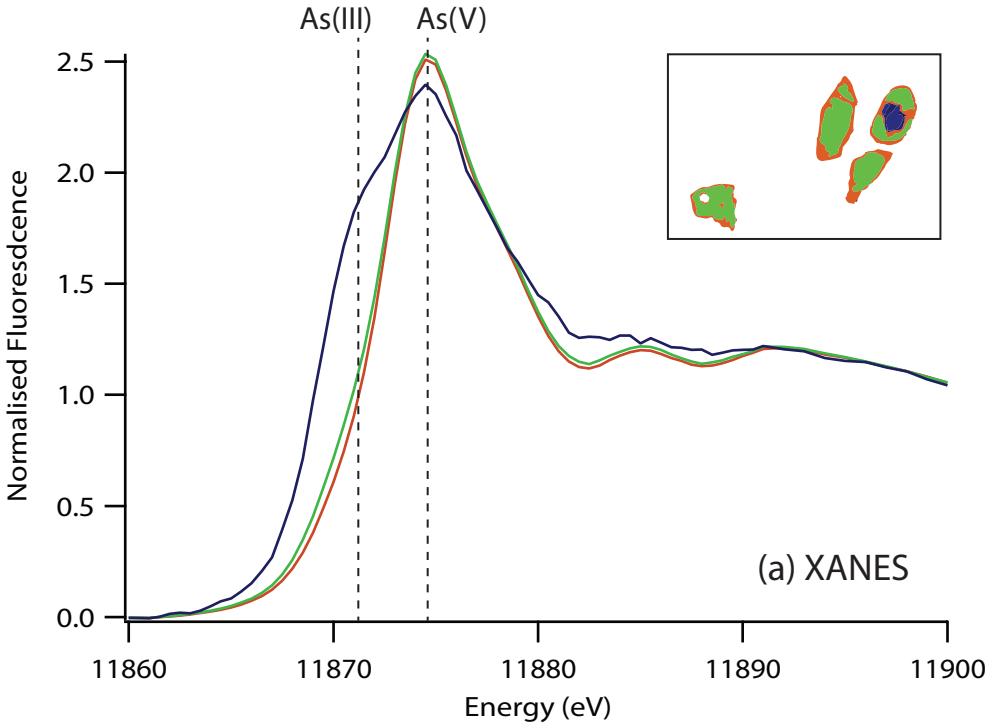

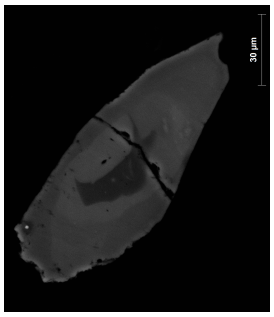

(a) BSE

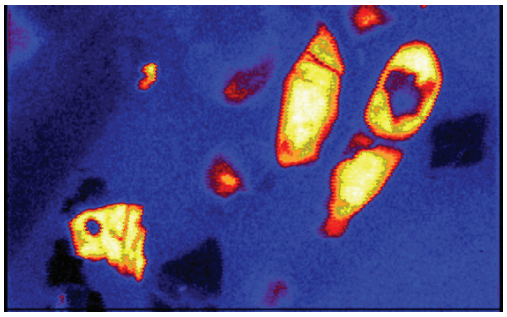

(c) XFM As 0 3.7%

Fig 12

Figure 13

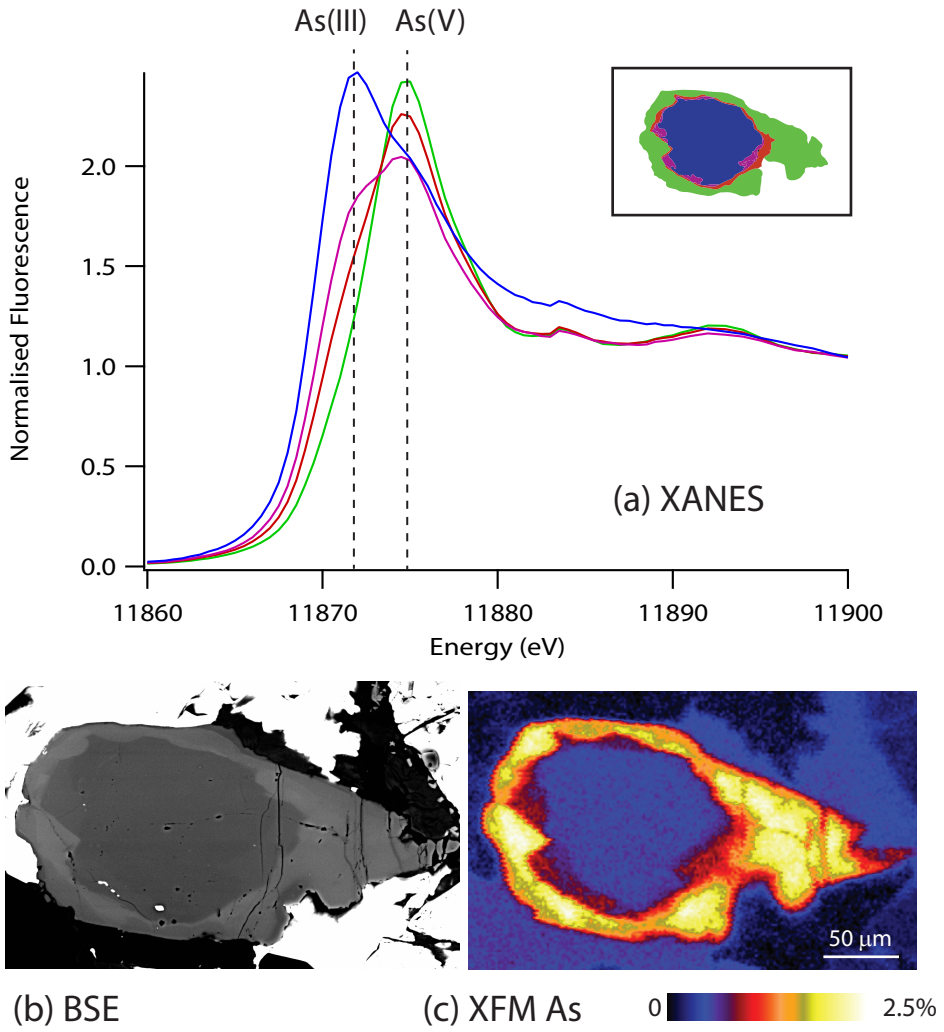

Fig. 13